

High-Resolution Data Assimilation for Two Maritime Extreme Weather Events: A comparison between 3DVar and EnKF.

Diego S. Carrió¹, Vincenzo Mazzearella², Rossella Ferretti²

¹Meteorology Group, Department of Physics, University of the Balearic Islands, Palma, Spain

²CETEMPS, Department of Physical and Chemical Sciences, University of L'Aquila, L'Aquila 67100, Italy

Abstract

Populated coastal regions in the Mediterranean are known to be severely affected by extreme weather events. Generally, they are initiated over maritime regions, where a lack of in-situ observations is present, hampering the initial conditions estimations and hence, the forecast accuracy. To face this problem, Data Assimilation (DA) is used to improve the estimation of the initial conditions and their respective forecasts. Although comparisons between different DA methods have been performed at global scales, few studies are performed at high-resolution, focusing on extreme weather events triggered over the sea and enhanced by complex topographic regions. In this study, we investigate the role of assimilating different types of conventional and remote-sensing observations using the variational 3DVar and the ensemble-based EnKF, which are of the most common DA schemes used globally at National Weather Centers. To this aim, two different events are chosen because of both the different areas of occurrence and the triggering mechanisms. Both the 3DVar and the EnKF are used at convection permitting scales to improve the predictability of these two high-impact coastal extreme weather episodes, which were poorly predicted by numerical weather prediction models: (a) the heavy precipitation event IOP13 and (b) the intense Mediterranean Tropical-like cyclone Qendresa. Results show that the EnKF and 3DVar perform similarly for the IOP13 event for most of the verification metrics, although looking at the ROC and AUC scores, the EnKF clearly outperforms the 3DVar. However, the ensemble mean of the EnKF is in general worse than the 3DVar for Qendresa, although some of the ensemble members of the EnKF individually outperforms the 3DVar allowing for gaining information on the physics of the event and hence the benefits of using an ensemble-based DA scheme.

Correspondence: Diego S. Carrió, University of the Balearic Islands, 07122, Cra. Valldemossa km 7.5, Balearic Islands, Palma (Spain)

Email: diego.carrio@uib.es

Keywords: Variational Data Assimilation (3DVar), ensemble data assimilation (EnKF), low-predictable weather events, extreme weather events, high-resolution numerical forecasts.

47

48 1. Introduction

49 The Mediterranean basin is recognized as one of the geographical regions most frequently
50 affected by high impact weather events in the world (Petterssen, 1956). The Mediterranean
51 region has a natural disposition for these events because of its singular orographic features,
52 which include having a relatively warm sea surrounded by complex terrain. This geographical
53 configuration forces the warm and moist airflow to lift, favoring condensation and triggering
54 convection. Hazardous weather events in this region, such as heavy precipitation (e.g., flash
55 floods, snowstorms), cyclogenesis or windstorms (e.g., squall lines, tornadic thunderstorms),
56 produce huge economic, injury and human losses in populated coastal regions (e.g., Romero et
57 al., 1998b; Llasat and Sempere-Torres, 2001; Llasat et al., 2010; Jansa et al., 2014; Flaounas
58 et al., 2016; Pakalidou and Karacosta, 2018; Amengual et al., 2021). Since 1900, more than
59 500 billion Euros associated with total damages to the property and over 1.3 million fatalities
60 related to hydrometeorological disasters has been registered for the EM-DAT international
61 disaster database¹. These effects underscore the critical need for accurate and rapid high-
62 resolution weather forecasting systems, aimed at extending the lead time for severe weather
63 warnings, thereby enabling the implementation of effective mitigation strategies to reduce
64 fatalities and economic losses. However, while the accuracy of weather forecasting has
65 significantly improved in recent years, with better representation of physical processes and
66 dynamics, accurate prediction of high impact weather events in terms of their location, timing,
67 and intensity remains a major challenge for the scientific community (Stensrud et al., 2009;
68 Mass et al., 2002; Bryan and Rotunno, 2005; Yano et al., 2018; Torcasio et al., 2021). For this
69 reason, improving the forecast of high-impact weather events becomes an imperative goal.

70 Deficiencies in the accurate prediction of the location (spatial and temporal), intensity and
71 phenomenology of extreme weather events are tightly related to the accuracy of the initial
72 conditions of the system (Wu et al., 2013). The initial conditions of the hazardous weather
73 events affecting coastal populated regions, are typically poorly estimated, mainly because these
74 weather systems originate over the sea, where there is a lack of *in-situ* observations. Enhanced
75 representations of the initial conditions are typically achieved by blending information from
76 observations into numerical models through sophisticated *Data Assimilation* (DA) techniques
77 (Kalnay, 2003), which accounts not only for the nominal values of the observations and the
78 model, but also accounts for their respective error statistics. DA has been widely used and
79 applied for global numerical weather prediction (NWP) problems (e.g., Eliassen, 1954; Lorenc,
80 1981; Le Dimet and Talagrand, 1986; Rabier et al., 2000, Whitaker et al., 2008, Carrassi et al.,
81 2018; Albergel, et al., 2020, among others). However, less attention has been paid to
82 convective-scale NWP problems, especially those associated with small scale convective
83 phenomena initiated over regions with sparse observational data coverage, such as the extreme
84 weather events affecting coastal regions in the Mediterranean basin (Carrió et al., 2016;
85 Amengual et al., 2017; Carrió et al., 2019; Lagasio et al., 2019; Amengual et al., 2021;
86 Mazzarella et al., 2021; Torcasio et al., 2021, Capecchi et al., 2021). To improve forecasts of
87 such extreme weather events, accurate high resolution numerical weather models which solve
88 convective scale processes are required, as well as dense observations at high spatial and
89 temporal resolution. These will provide accurate information regarding the convective systems
90 themselves or their environmental conditions. One of the most important sources of convective
91 scale information are ground weather radars that provide three-dimensional data related to the
92 storms at high spatial (order of hundreds of meters) and temporal (order of few minutes)

¹ <https://www.emdat.be/>

93 resolution. In addition, weather radars provide thermodynamic and dynamic information of
 94 thunderstorms, which are crucial to understand and forecast convective structures. Due to the
 95 high spatio-temporal variability of convective structures, a rapid update cycle of the initial state
 96 (i.e., analysis) using weather radar observations is required to reduce errors and keep physical
 97 balances in the initial conditions. Several studies have shown the positive impact in forecasting
 98 severe weather events by assimilating weather radar information (e.g., Xiao and Sun, 2007;
 99 Lee et al., 2010; Wheatley et al., 2012; Yussouf et al., 2015; Carrió et al., 2019; Mazzarella et
 100 al., 2021).

101 During the last decades, different DA algorithms have been developed with the aim of
 102 improving weather forecasts making use of all available observations in the best possible way.
 103 In this context, most of the developed DA methods are based on exploiting Bayes' Theorem
 104 (Lorenc, 1986) and making use of different types of approximations. Generally, DA algorithms
 105 can be classified into the following three Bayesian-based families: (a) Variational DA (e.g.,
 106 3DVar (Barker et al., 2004) or 4DVar (Huang et al., 2009)); (b) Ensemble-based DA, which
 107 are based on the *Ensemble Kalman Filter* (EnKF; Evensen, 1994) and (c) Monte-Carlo DA
 108 methods. Variational DA minimizes a cost function to obtain the analysis (i.e., the best
 109 estimation of the initial conditions). More specifically, variational DA methods provide a
 110 (quasi) optimal analysis based on an imperfect forecast (*prior* state or *background*), a set of
 111 imperfect observations and their respective error statistics that are prescribed and assumed to
 112 be Gaussian, for simplicity. In addition, variational DA algorithms require a linearized and
 113 adjoint version of the numerical model, which can be very difficult to develop and maintain.
 114 This often involves the use of automatic differentiation tools or complex manual derivation,
 115 both of which are error-prone and time-consuming. On the other hand, the ensemble-based DA
 116 algorithms do not require the use of linearized or adjoint versions of the model, and they do
 117 not use prescribed error statistics. Instead, they compute the error statistics from an ensemble
 118 of forecasts, with the main property that these errors are evolving in time as the system evolves.
 119 The Monte-Carlo DA method allows the assimilation of observations described with non-
 120 Gaussian errors. Particle filters (PF; Van Leeuwen, 2009; Poterjoy, 2016) are a clear example
 121 of Monte-Carlo DA algorithm. However, PFs are not well-suited for large multidimensional
 122 systems, such as the atmosphere, although a lot of improvements have been achieved recently.
 123 In the present study, we will focus on the most widely used DA schemes typically used in major
 124 operational weather centers, which are the variational and ensemble-based DA schemes,
 125 leaving the Monte-Carlo methods for future work.

126 Although variational DA schemes have been used in numerical weather prediction for many
 127 years (Courtier et al., 1994; Park and Zupanski, 2003; Rawlins et al., 2007), allowing the
 128 assimilation of a wide range of different observations, they present a well-known limitation.
 129 This limitation is related to the use of a climatological background error covariance matrix to
 130 characterize the error statistics, which is kept constant along the assimilation window, where
 131 the different observations are distributed at different times. This weakness is specifically linked
 132 to the 3DVar method, which typically uses the *National Meteorological Center* (NMC) method
 133 (Parrish and Derber, 1992) to generate those static background error covariances using forecast
 134 differences over a period of time reasonably close to the event. The error statistics derived from
 135 such DA schemes are static, isotropic and nearly homogenous, misrepresenting the true error
 136 statistics in space and time, which are inherently flow-dependent, resulting in less accurate
 137 analysis. On the other hand, the EnKF DA scheme is designed to provide flow-dependent
 138 background error covariances. Some studies have shown the potential of the EnKF spreading
 139 information from the observations flow-dependently in comparison with the 3DVar (Yang et
 140 al., 2009; Gao et al., 2018). On the other hand, 3DVar techniques require less computational
 141 resources and there is no need to build an ensemble compared to EnKF or even simulate the

142 model trajectory as in 4DVar. Therefore, the assimilation with 3DVar takes only a few tens of
143 minutes, making this technique particularly suitable for operational purposes.

144 To resolve convective scale (i.e., grid spacing of a few kilometers) physical processes
145 associated with extreme weather phenomena, high-resolution numerical simulations are
146 required, as well as high resolution initial conditions. This turns in performing computational
147 expensive high-resolution simulations, which poses a significant challenge by limiting the
148 number of ensemble members that can be used in EnKF DA schemes, potentially hindering the
149 estimation of the background error covariance matrix. Determining which DA method yields
150 greater accuracy – 3DVar using an ad hoc background error covariance matrix versus EnKF
151 with a flow-dependent low-rank background error covariance derived from a finite ensemble –
152 remains challenging under constrained computational resources.

153 Recent convective-scale DA studies have primarily focused on the mature stage of weather
154 events (e.g., Tong et al., 2005; Fujita et al., 2007; Dowell et al., 2021; Jones et al., 2013;
155 Wheatley et al., 2015; Jones et al., 2016; Gao et al., 2016; Ballard et al., 2016; Gustafsson et
156 al., 2018; Carrió et al., 2019; Mazzarella et al., 2020; Yussouf et al., 2020; Federico et al.,
157 2021; Junjun et al., 2021; Janjić et al., 2022; Wang et al., 2022). However, at this stage, the
158 system is already well-developed and likely impacting the population, limiting the
159 effectiveness of DA in terms of forecast lead time. In such cases, the potential for early
160 warnings and mitigation actions is significantly reduced, as there is little time left to respond
161 and minimize socio-economic impacts. Despite its potential benefits, only a handful of studies
162 have explored the impact of DA using high-resolution numerical models in the developing
163 stage (e.g., Carrió et al., 2019; Carrió et al., 2022; Corrales et al., 2023), and even fewer have
164 done so over data-sparse maritime regions, where early assimilation could be most valuable,
165 providing advanced warnings and allowing decision-makers to act proactively. This study fills
166 that gap by directly comparing two widely used DA techniques – 3DVar and EnKF – in high-
167 resolution, pre-convective assimilation experiments for two extreme weather events initiated
168 over the sea affecting populated coastal regions in the Mediterranean basin. It is important to
169 emphasize that this study does not aim to derive statistically significant conclusions. Instead,
170 the main objective is to compare the performance of EnKF and 3DVar in two distinct extreme
171 weather events, each characterized by unique atmospheric conditions and observational
172 limitations. The two extreme weather events selected for this study are: (a) the heavy rainfall
173 episode, IOP13, affecting coastal regions of Italy during October 2012 (Pichelli et al., 2017)
174 and (b) the low-predictable Mediterranean Tropical-like cyclone (medicane), Qendresa,
175 affecting Sicily in November 2014 (Pytharoulis et al., 2017; Pytharoulis, 2018; Cioni et al.,
176 2018; Di Muzio et al., 2019).

177 On overall, this study aims at:

178 (a) Assessing the impact of 3DVar in comparison with the EnKF system to predict small-scale
179 extreme weather events initiated over maritime regions with lack of *in-situ* observations.

180
181 (b) Compare the forecast impact from assimilating *in-situ* conventional observations in
182 comparison to assimilating high spatial and temporal resolution data from remote sensing
183 instruments.

184
185 (c) Provide a quantitative assessment between the different DA schemes by means of using
186 several statistical verification methods.

Eliminado: In this context, which DA method is more suitable?

Eliminado: Given limited computational resources, it is unclear which DA method is more accurate.

Eliminado: The 3DVar using an *ad hoc* background error covariance matrix or the low-rank background error covariance matrix obtained from the EnKF?

Eliminado: However, at this stage, the system is already well-developed and likely impacting the population, limiting the effectiveness of DA in terms of forecast lead time. In such cases, the potential for early warnings and mitigation actions is significantly reduced, as there is little time left to respond and minimize socio-economic impacts. Despite its potential benefits, very few studies have explored the role of DA in the developing stage (e.g., Carrió et al., 2019; Carrió et al., 2022; Corrales et al., 2023), where assimilating observations before convection initiates could significantly improve forecast lead time, providing advanced warnings and allowing decision-makers to act proactively. In this study, we compare the performance of two widely used DA techniques – 3DVar and EnKF – in enhancing the forecast lead time for two extreme weather events initiated over the sea, a data-sparse region where observational constraints pose additional forecasting challenges, affecting populated coastal regions in the Mediterranean basin.

Eliminado: However, at this stage, the system is already well-developed and likely impacting the population, limiting the effectiveness of DA in terms of forecast lead time. In such cases, the potential for early warnings and mitigation actions is significantly reduced, as there is little time left to respond and minimize socio-economic impacts. Despite its potential benefits, only a handful of studies have explored the impact of DA using high-resolution numerical models in the developing stage (e.g., Carrió et al., 2019; Carrió et al., 2022; Corrales et al., 2023), and even fewer have done so over data-sparse maritime regions, where early assimilation could be most valuable, providing advanced warnings and allowing decision-makers to act proactively. This study fills that gap by directly comparing two widely used DA techniques – 3DVar and EnKF – in high-resolution, pre-convective assimilation experiments for two extreme weather events initiated over the sea affecting populated coastal regions in the Mediterranean basin

Eliminado: (b)

Eliminado:

Eliminado: Investigate the potential of using 3DVar and EnKF in the developing phase, specifically 12 hours before the mature stage of convective systems are reached, to improve forecast lead time.

Eliminado: Investigate the potential of using 3DVar and EnKF in the developing phase,

Eliminado: 12

Eliminado: that is hours before the mature stage of convective systems are reached, to improve forecast lead time and warning capabilities for extreme weather events.

Eliminado: c

Eliminado: d

244
245 This paper is organized as follows. Section 2 briefly describes the meteorological
246 characteristics of the two events used for comparing the impact of 3DVar and EnKF. In Section
247 3 the observation dataset that will be assimilated by the different DA methods will be presented.
248 Section 4 briefly explains the main characteristics of the two DA algorithms that will be used
249 in this study. Then, the numerical model configuration and the design of the different
250 experiments for the two different case studies will be described in Section 5 and 6, respectively.
251 Section 7 describes the verification methods used in this study. Results of the different
252 numerical experiments for both meteorological situations are summarized in Section 8. Finally,
253 conclusions are presented in Section 9.

254

255

256 **2. Brief Description of Case Studies**

257

258 Two different extreme weather systems, occurring in the Mediterranean region and affecting
259 populated coastal regions, are considered in this study. The first extreme weather event was
260 associated with heavy rainfall affecting central and northern Italy during October 2012
261 (IOP13), while the second extreme weather event was associated with the Qendresa medicane
262 affecting southern Sicily, Lampedusa, Pantelleria and Malta islands during November 2014.
263 Both systems were poorly forecasted, making them perfect candidates for this intercomparison
264 study to assess the impact of data assimilation techniques.

265

266 **2.1. The IOP13 Heavy Precipitation Episode**

267

268 The *IOP13* occurred during the *First Special Observation Period* (SOP1) of the international
269 project *Hydrological cycle in the Mediterranean Experiment* (HyMeX; Drobinski et al., 2014),
270 that was mainly designed to better understand heavy rainfall and flash flooding episodes
271 occurring in the Mediterranean region. The heavy precipitation IOP13 event took place
272 between 14 and 16 October 2012, and it was characterized by a frontal precipitation system
273 associated with a deep upper-level trough extending from northern France towards northern
274 Spain (Fig. 1). It initially affected southern France coastal areas, and afterward it also affected
275 the northern and central parts of Italy. During 15 October, the Italian rain gauge network
276 registered 24-hour accumulated precipitation with peaks reaching 60 mm in central Italy, 160
277 mm in northeastern Italy and 120 mm in Liguria and Tuscany. During the night of 14 October,
278 a cold front affected the Western Mediterranean region and during 15 October the system
279 rapidly moved from France to Italy, advecting low-level moisture towards the western coast of
280 Italy and Corsica, destabilizing the atmosphere and favoring deep moist convective activity.
281 More details on the synoptic situation and observational data collected during IOP13 can be
282 found in Ferretti et al., 2014.

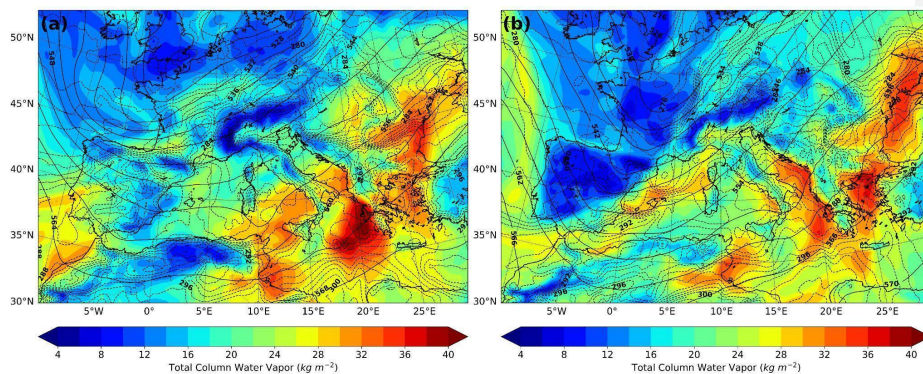


Figure 1. IOP13 ERA5 analyses: 500 hPa geopotential (solid black lines), 925 hPa temperature (dashed grey lines) and total column of water vapor (color shaded areas) at (a) 12 UTC 14 October and (b) 00 UTC 15 October 2012.

2.2. The Qendresa Tropical-Like Cyclone Episode

Among the wide spectrum of maritime extreme weather events, tropical-like Mediterranean cyclones, a.k.a. medicanes (Emmanuel, 2005), draw particular attention to the community mainly because they share similar morphological characteristics with tropical cyclones. Given their tendency to impact densely populated and economically critical areas around the Mediterranean basin, enhancing the accuracy and reliability of medicanes forecasts has become an urgent priority. Here, we focus on the 7 October 2014 medicanes (Qendresa; Cioni et al., 2018) that affected the islands of Lampedusa, Pantelleria, Malta and the eastern coast of Sicily. This event was recognized by the community for its limited predictability (Carrió et al., 2017), making it a compelling case study for investigating the performance of the 3DVar and EnKF DA methods. *In-situ* observations located in Malta's airport registered gust wind values exceeding 42.7 m s^{-1} and a sudden and deep pressure drop greater than 20 hPa in 6 hours. Satellite imagery during its mature phase showed a well-defined cloud-free eye surrounded by axisymmetric convective activity, which resembles the morphological properties of classic tropical cyclones.

A deep upper-level trough associated with a cyclonic flow at mid-levels characterized the synoptic situation in the Western Mediterranean from 5 to 8 November 2014. The upper-level trough was associated with an intense PV streamer extending from Northern Europe to Southern Algeria, and the cyclonic flow at mid-levels was dominated by a strong ridge over the Atlantic and a deep trough moving along Western Europe. Late on 7 November, the upper-level trough became negatively tilted, evolving into a deep upper-level cut-off low and the PV streamer disconnected from the northern nucleus (Fig. 2). A small well-defined spiral-to-circular cloud shape formed just south of Sicily and evolved east-northeastward, reaching its maximum intensity over Malta, at midday. Finally, the cyclonic system dissipated as it crossed the Catania (eastern) coast of Sicily. More details on the synoptic situation and observational data collected during this event can be found in Carrió et al., 2017.

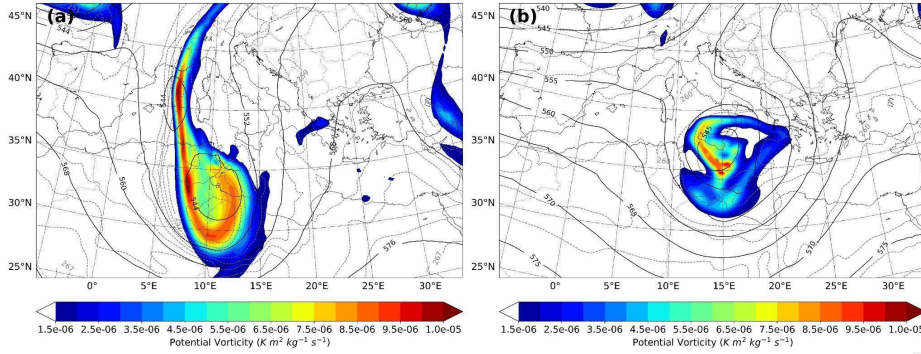


Figure 2. Qendresa ERA5 analyses: 500 hPa geopotential (solid black lines), 500 hPa temperature (dashed grey lines) and 300 hPa Potential Vorticity (color shaded areas) at (a) 00 UTC 7 November and (b) 00 UTC 8 November 2014.

3. Observations Description

In this study, a combination of remote-sensing and *in-situ* observations were assimilated for both case studies. Specifically, the following three types of observations were assimilated: (a) conventional *in-situ* data from surface meteorological stations, maritime buoys, rawinsondes and aircraft measurements, (b) high temporal and spatial reflectivity data from two Doppler Weather Radars and (c) satellite-derived 3D wind speed and direction data. A summary of the assimilated observations, including their data sources, assimilation frequency, coverage and additional processing is provided in Table 1.

Event	Observation Type	Data Sources	Assimilation Frequency	Coverage	Additional Processing
IOP13	Conventional <i>in-situ</i> data	MADIS (NOAA)	Hourly	Entire Domain	Quality-controlled
IOP13	Radar Reflectivity	Météo-France Doppler Weather Radars (Aleria & Nîmes)	Every 15 minutes	Ligurian Sea & Gulf of Genoa	Quality controlled and Interpolated using Cressman Objective Analysis (6 km grid)
Qendresa	Conventional <i>in-situ</i> data	MADIS (NOAA)	Hourly	Mediterranean Region	Quality-controlled
Qendresa	Satellite-Derived Winds (RSAMVs)	EUMETSAT (SEVIRI instrument onboard MSG)	Every 20 minutes	Entire atmosphere over the Mediterranean Region	Quality-controlled, superobbing (128x128 km, 25 hPa vertical)

Table 1: Summary of assimilated observations for each case study, including observation type, data sources, assimilation frequency, spatial coverage and additional processing details.

3.1. IOP13 Observations

For the IOP13, we assimilated both *in-situ* conventional data and remote sensing observations from two Doppler Weather Radars. While Italy has a dense national network of radar and *in-situ* stations, the majority of these datasets were not publicly available. To ensure

reproducibility and accessibility, we exclusively used freely available data. For radar observations, we assimilated data from the only two radars providing coverage over the maritime region where the event initiated. Specifically, data from: (a) Aleria radar (9.496°E, 42.129°N, 63 m ASL), located on Corsica Island, and (b) Nimes radar (4.502°E, 43.806°N, 76 m ASL), located in southern France (Fig. 3a). These two Météo-France polarimetric S-band Doppler Weather Radars, strategically positioned, ensure a good spatial coverage over the Ligurian Sea, the area where triggering and intensification of deep convection occurred, and provide key information about the 3D structure of the convective systems at high spatial and temporal resolution. Aleria and Nimes radars perform 5 and 9 elevation scans every 5 minutes, respectively, and their data are available at the HyMeX's official website (see <https://www.hymex.org>). Specifically, Aleria radar provides data at 5 elevation angles: 0.57°, 0.96°, 1.36°, 3.16° and 4.57° with a mean frequency of 2.8 GHz. In comparison, Nimes radar provides data at 9 elevation angles: 0.58°, 1.17°, 1.78°, 2.38°, 3.49°, 4.99°, 6.5°, 7.99° and 89.97°, also at the same frequency. It is worth mentioning that Aleria and Nimes radar reflectivity data are provided by the Météo-France operational radar network and undergo rigorous data quality control. This ensures that common radar error sources, such as signal attenuation, ground clutter or beam blocking, are meticulously identified and corrected. Radial velocity from Aleria and Nimes Doppler radars was also available, but because of the low reliability of the data (not quality controlled properly) it was not used in this study. Additionally, conventional *in-situ* observations were obtained from NOAA's Meteorological Assimilation Data Ingest System (MADIS), a global dataset that provides high-quality, quality-controlled meteorological observations. In particular, we assimilated pressure, temperature, humidity and horizontal wind speed and direction from *in-situ* instruments such as METARs, maritime buoys, rawinsondes and aircrafts (Fig. 3a).

Overall, the following observations were assimilated for this event:

- Conventional *in-situ* data were hourly assimilated over the entire model domain (Fig. 3a).
- Reflectivity data from Aleria and Nimes weather radars were assimilated every 15 minutes (Fig. 3a).

The high spatial resolution of the reflectivity data poses significant challenges for their direct assimilation, potentially leading to detrimental analysis related with signal aliasing and the violation of the uncorrelated observational error assumptions followed in the derivation of the 3DVar and EnKF analysis equations. To mitigate the adverse effects associated with these issues, the *Cressman Objective Analysis* technique (Cressman, 1959) was used to interpolate raw radar observations to a regularly spaced 6 km horizontal grid, as suggested by previous work (i.e., Wheatley et al., 2015; Yussouf et al., 2015). It is important to note that reflectivity observations are typically obtained in polar coordinates, a prerequisite step before applying the Cressman interpolation involves converting them to a Cartesian coordinate system. We have performed several sensitivity tests using different grid space resolution (e.g., 3, 6, 9 km) and we found that using 6 km grid space produces the best analysis. To reduce spurious convective signals and remove excessive humidity the *null-echo* option, which allows assimilation of no precipitation echoes, has been adopted in 3DVAR experiment.

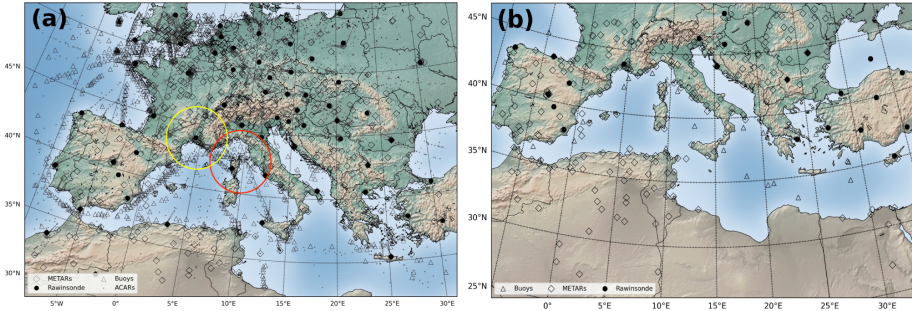


Figure 3. (a) IOP13 Episode: Spatial distribution of in-situ observations (gray and black markers) assimilated on the parent numerical domain during 24 h assimilation window from 00 UTC 14 October to 00 UTC 15 October 2012. Doppler Weather Radars located at Nimes and Aléria and their coverage range, depicted in yellow and red circles, respectively. (b) Qendresa Episode: Spatial distribution of in-situ observations hourly assimilated during 12 h assimilation window from 12 UTC 6 November to 00 UTC 7 November 2014.

3.2. Qendresa Observations

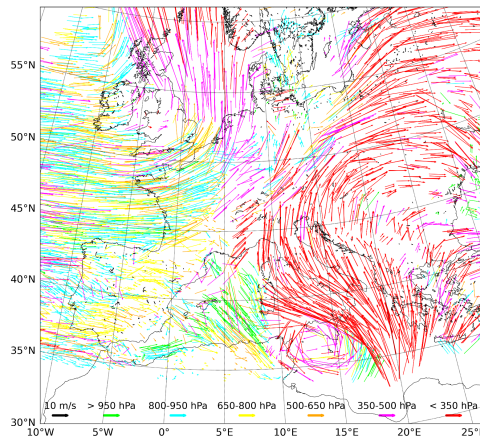
For the Qendresa event, two different observational sources were publicly available: (a) conventional *in-situ* observations and (b) satellite-derived observations. Conventional *in-situ* observations were obtained from MADIS database. However, only observations from buoys, METAR and rawinsonde were used for this case. It is essential to highlight that observation gaps persist across large areas of the region, particularly over the sea (Fig. 3b), where Qendresa initiated and evolved. As for the IOP13, we were interested in Doppler Weather Radars data to enhance the intensity and trajectory forecasts of Qendresa. Unfortunately, Doppler Weather Radars were not publicly available in the neighborhood of the region where Qendresa initiated and evolved. Instead, we used an alternative high-resolution data source, the so-called *Rapid-Scan Atmospheric Motion Vectors* (RSAMVs; Velden et al., 2017). This dataset provides 3D wind information throughout the entire atmosphere (both speed and direction) at high spatial and temporal resolution (i.e., every 20-min). These observations were particularly valuable for capturing wind field structures over the sea, where conventional observations were sparse or unavailable. This satellite product is obtained using the *Spinning Enhanced Visible and Infrared Imager* (SEVIRI) instrument onboard the *Meteosat Second Generation* (MSG) satellite, which has a scanning frequency as low as 5 minutes. The final product is indeed obtained averaging 4 consecutive images.

Hence, the following observations were assimilated for this event:

- Conventional *in-situ* data from buoys, METAR and rawinsonde for the entire Mediterranean region were hourly assimilated.
- Wind speed and direction from the *Rapid-Scan Atmospheric Motion Vectors* for the entire atmosphere at high spatial and temporal resolution were assimilated every 20 minutes.

Recent studies have shown that upper-level dynamics played a key role in the genesis and the development of Qendresa (Carrió et al., 2017; Carrió, 2022), so the assimilation of RSAMVs is expected to significantly improve its predictability. Here, the infrared channel from

426 RSAMVs ($10.8\ \mu\text{m}$), which contains information throughout the entire atmosphere, was
 427 selected to be assimilated (Fig. 4). However, before assimilating RSAMVs, a quality control
 428 check to reject non-physical and outlier observations that could deteriorate the quality of the
 429 analysis and the successive forecast was applied. In addition, to minimize the effect of having
 430 spatial correlated observation errors associated to high density observations, the “superobbing”
 431 technique consisting in reducing the data density through spatially averaging the observations
 432 within a predefined prism is applied (i.e., Pu et al., (2008); Romine et al., (2013); Honda et al.,
 433 (2018)). Based on the most accurate analysis obtained by multiple sensitivity experiments (not
 434 shown) for Qendresa, the RSAMVs data are thinned using a prism with horizontal resolution
 435 of $128 \times 128\ \text{km}^2$ and 25 hPa in the vertical.



436 **Figure 4.** Raw EUMETSAT’s RSAMV observations depicted at different vertical levels by infrared channel $10.8\ \mu\text{m}$ at 12 UTC on 7 November 2014 over the Mediterranean region. Wind information is only valid at the center
 437
 438 of the wind vectors.
 439
 440
 441

442 Observations from aircraft (i.e., ACARS) were not assimilated in this case because preliminary
 443 assimilation tests indicated a worsening of the results and led to a poorer estimation of the
 444 atmospheric state. Buoys, METAR and rawinsonde observations covering the entire
 445 Mediterranean region were hourly assimilated.

446 Finally, observational errors used for the assimilation of the observations associated with both
 447 IOP13 and Qendresa are motivated by Table 3 in Romine et al., (2013) with the following
 448 minor changes: METAR altimeter (1.5 hPa), marine altimeter (1.20 hPa), METAR and marine
 449 temperature (1.75 K) and RSAMV wind observations ($1.4\ \text{m s}^{-1}$). These minor changes are
 450 found to provide better data assimilation analysis for the IOP13 and Qendresa extreme weather
 451 events in the Mediterranean region. The remaining of the observation errors are the same as
 452 the ones in Romine et al., (2013).

453

454

455 4. Data Assimilation Schemes

456

457 In the present study, two widely used data assimilation algorithms are used for improving the
 458 forecast of extreme weather events initiated and developed over poorly observed maritime

regions and affecting densely populated coastal areas. We refer to the *Ensemble Adjustment Kalman Filter* and the variational *3DVar* data assimilation schemes, which are briefly described below.

a) The Ensemble Adjustment Kalman Filter (EnKF)

The *Ensemble Adjustment Kalman Filter* (EAKF; Anderson 2001), which is implemented in the *Data Assimilation Testbed Research* (DART²), is used in this study as the former ensemble-based data assimilation technique. The EAKF provides an optimal estimation, in the least square error sense, of the true probability distribution of the state of the atmosphere by merging two main sources of information: (a) the available observations and (b) an ensemble of forecasts (a.k.a. *background*) valid at the analysis time. In particular, the EAKF assimilates the observations serially. This means that the analysis ensemble obtained by the EAKF after the assimilation of the first observation at a given time is then used as the *background* for the next observation at the same analysis time. This is done recursively until all the observations valid at the same analysis time are finally assimilated.

Ensemble covariances used in real case studies, where only a limited number of ensemble members is feasible, suffers from sampling error, resulting in the generation of spurious correlations that hamper the analysis (Hacker et al., 2007). The detrimental effects of these spurious correlations are mitigated by employing covariance localization functions that go to zero as the distance between the assimilated observation and the grid model point where the analysis occurs, increases (Houtekamer and Mitchell, 1998). In our case, a fifth-order piecewise rational Gaussian localization function is used (Gaspari and Cohn, 1999). For this study, after several sensitivity simulations it was found that using a half-radius³ of 230 km in the horizontal and a half-radius of 4 km in the vertical for the horizontal and vertical localizations, respectively, results in the best performance of the DA scheme.

Assimilating observations inherently reduces analysis variance in both variational and Kalman filter frameworks. Small ensemble sizes tend to overly collapse the ensemble spread (Anderson and Anderson, 1999). To mitigate this underdispersion, and maintain realistic ensemble variance, a spatially varying adaptive inflation technique (Anderson and Collins, 2007; Anderson et al., 2009) is applied to the prior ensemble before assimilating the observations. This adaptive inflation technique increases the spread of the ensemble without changing the mean. The inflation value has a probability density distribution described by a mean and a standard deviation. In this study, it was determined that initializing the mean value of inflation at 1.0 and using a standard deviation of 0.6, yields the best performance of the DA scheme.

b) Three-dimensional Variational Data Assimilation (3DVar)

- Eliminado: The assimilation of each observation results in a reduction of the ensemble spread, attributed to using a reduced-moderate ensemble size
- Eliminado: address
- Eliminado: issue
- Eliminado: help to
- Eliminado: the spread
- Eliminado: n
- Eliminado: c

² <http://www.image.ucar.edu/DARes/DART/>
³ The half-radius or cutoff term is defined here as 0.5 times the distance to where the impact of the observation assimilated go to zero. Multiplying the half-radius by 2 results in the maximum distance at which an observation can modify the model state.

The 3DVar technique, implemented in WRFDA (Barker et al., 2004), is adopted for the numerical simulations. The 3DVar aims to seek the best estimate of the initial conditions through the iterative minimization of a cost function:

$$J(\mathbf{x}) = \frac{1}{2} \left\{ (\mathbf{x} - \mathbf{x}_b)^T \mathbf{B}^{-1} (\mathbf{x} - \mathbf{x}_b) + [\mathbf{y}_o - \mathbf{H}(\mathbf{x})]^T \mathbf{R}^{-1} [\mathbf{y}_o - \mathbf{H}(\mathbf{x})] \right\}$$

where \mathbf{B} and \mathbf{R} are the background and observation error matrices, respectively; \mathbf{x} is the state vector; \mathbf{y}_o is the observations, \mathbf{x}_b is the first guess and H is the forward (non-linear) operator that converts data from model space to observation space.

The solution of the above cost function J consists in finding a state \mathbf{x}_a (analysis), that minimizes the distance between the observations and the background field. However, in a model with 10^6 degrees of freedom, the direct solution is computationally expensive. To reduce the complexity and calculate \mathbf{B}^{-1} more efficiently, a pre-conditioning is applied by transforming the control variables, respectively, pseudo relative humidity, temperature, u , v , and surface pressure, as $\mathbf{x} - \mathbf{x}_b = \mathbf{U}\mathbf{v}$, where \mathbf{v} is the control variable and \mathbf{U} the transformation operator.

The background error covariance matrix \mathbf{B} matrix plays a key role in the assimilation process by weighing and smoothing the information from observations and by ensuring a proper balance between the analysis fields. The *National Meteorological Center* method (NMC; Parrish and Derber, 1992) was used to model the \mathbf{B} matrix. This method evaluates the differences between two short-term forecasts valid at the same time but with different lead time, 12h and 24h, respectively, to generate the forecast error covariance matrix \mathbf{B} . In this study, we build the 3DVar \mathbf{B} matrix over a two-week period, in line with our operational experience running 3DVar and previous demonstrations of its benefits (Hung et al. 2023; Fitzpatrick et al., 2007; Mazzarella et al., 2020, 2021). To enhance \mathbf{B} 's quality despite this relatively short sampling window, we activate the CV7 option in WRFDA. This option uses empirical orthogonal functions (EOFs) to represent vertical covariances instead of the traditional recursive filter, which has proven particularly beneficial for radar-reflectivity assimilation and subsequent precipitation forecast improvements (Wang et al., 2013; Li et al., 2016; Shen et al., 2022; Ferrer Hernandez et al., 2022). In our configuration, the CV7 control variables (i.e., u , v , temperature, pseudo-relative humidity and surface pressure), are defined in EOF space, ensuring a compact yet accurate representation of error structures. We use the CV7 option to generate the \mathbf{B} matrix for both case studies. In addition, the weak penalty constraint (WPEC) option (Li et al., 2015) in WRFDA has also been activated to further improve the balance between the wind and thermodynamic state variables, enforcing the quasi-gradient balance on the analysis field.

5. Model set-up

The mesoscale Advanced Research Weather Research and Forecasting Model (WRF; Skamarock et al., 2008) version 3.7 is used in this study. WRF solves a fully compressible and non-hydrostatic set of equations, using a η terrain-following hydrostatic-pressure vertical coordinate. The Arakawa C-grid staggering scheme and a third-order Runge-Kutta time-integration, to improve the precision of the numerical solutions, are used. Because IOP13 and Qendresa episodes took place in different locations and with different conditions, two different model configurations were used. For the IOP13 episode, a one-way nested model configuration with the parent domain centered over the Western Mediterranean Sea, covering Central Europe and North Africa, with a horizontal grid-resolution of 15 km (168x247) and a nested domain

Con formato: Fuente: Negrita

Con formato: Fuente: Negrita

Con formato: Fuente: Negrita

Eliminado: Consistent with several papers (Hung et al. 2023; Fitzpatrick et al., 2007; Mazzarella et al.,

2020, 2021) showing positive results, a two-week period was used for the calculation of the \mathbf{B} matrix in this study. Recently, several works (Wang et al., 2013; Li et al., 2016; Shen et al., 2022; Ferrer Hernandez et al., 2022) show the benefit of using a slightly different approach for the \mathbf{B} matrix (CV7) in assimilating radar reflectivity, besides in precipitation forecast accuracy. The CV7 differs from the others by using empirical orthogonal functions (EOFs) to represent the vertical covariance instead of a vertical recursive filter. Moreover, the control variables are in eigenvector space, and they are the following: u , v , temperature, pseudo relative humidity (RH_e), and surface pressure (P_s). Therefore, CV7 option has been used to generate the \mathbf{B} matrix for both case studies. In this study, the weak penalty constraint (WPEC) option (Li et al., 2015) implemented in WRFDA has been activated to improve the balance between the wind and thermodynamic state variables, enforcing the quasi-gradient balance on the analysis field.

Eliminado: ¶

centered over Gulf of Genoa with a horizontal grid-resolution of 3 km (250x250) were used (Fig. 5a). 51 vertical model levels, from surface to 50 hPa, with higher density of levels in the lower part of the atmosphere than in the upper for both domains were used. For Qendresa, a one-way nested model configuration is also used, but now the parent domain is centered over the Central Mediterranean Sea, covering most of the European region and the northern part of Africa (Fig. 5b), using a horizontal grid resolution of 15 km (245x245). The nested domain is centered over Sicily (Southern Italy) using a grid resolution of 3 km (253x253). Both numerical domains use a 51 terrain-following η levels up to 50 hPa, as in the IOP13 case.

For the EnKF DA experiments, initial and boundary conditions used to perform the simulations associated with IOP13 were obtained from the *European Center of Medium Range Weather Forecasts Global Ensemble Prediction System* (EPS-ECMWF), which stored meteorological fields using a horizontal and vertical spectral triangular truncation of T639L62 (i.e., ~32 km grid resolution in the horizontal). In particular, the EPS-ECMWF provides 51 different initial and boundary conditions from 50 perturbed ensemble members plus a control simulation. However, due to unfeasible computational resources required to run our numerical simulations at high resolution, here we will use an ensemble consisting of 36 members. This configuration is analogous to the one used at the internationally prestigious *National Oceanic and Atmospheric Administration - National Severe Storms Laboratory* (NOAA-NSSL) in Norman (Oklahoma, USA) to improve predictability of tornadoes. To obtain the desired 36-member ensemble, a *Principal Components Analysis* and *K-mean* clustering technique were used together to select the 36 ensemble members from the EPS-ECMWF showing more dispersion over the entire numerical domain (see Garcies and Homar, 2009 and Carrió et al., 2016 for more details using these techniques). To perform Qendresa DA simulations, the initial and boundary conditions were obtained following the same methodology explained above for the IOP13 case, i.e., using an ensemble of 36 members obtained from the EPS-ECMWF. On the other hand, the initial and boundary conditions for 3DVar simulations are provided by the *Integrated Forecast System* (IFS) global model from the ECMWF, with a spatial resolution of $0.1^\circ \times 0.1^\circ$ and updated every 3 hours.

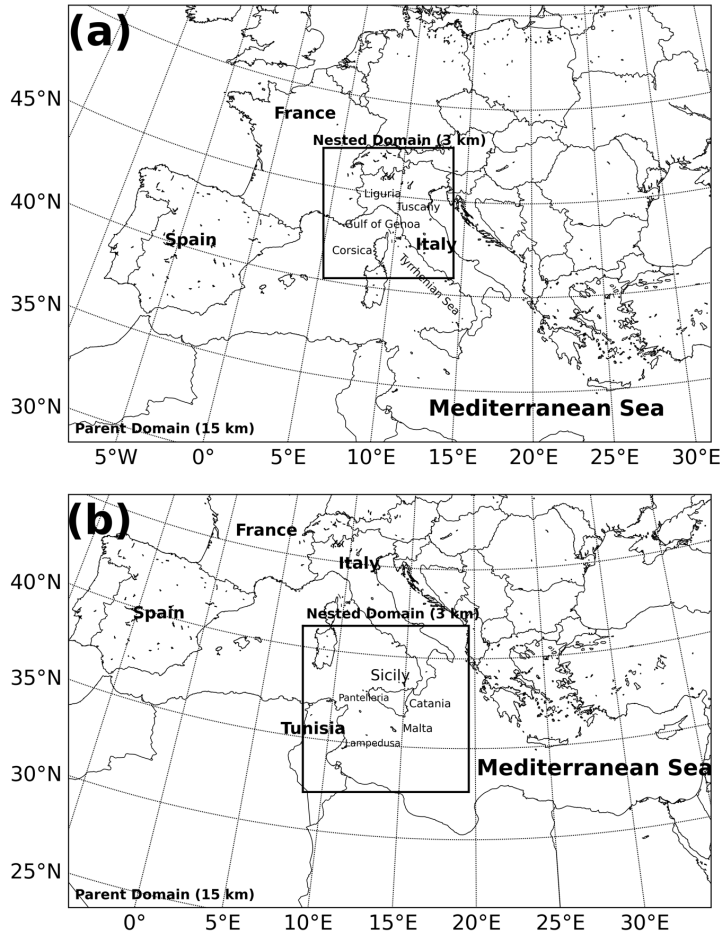


Figure 5. Meso- and storm-scale numerical domains used in this study for the (a) IOP13 and (b) Qendresa episodes, respectively.

To estimate the uncertainties of WRF, which is a necessary information for the EnKF, a multiphysics ensemble is built for both the IOP13 and Qendresa event (e.g., Stensrud et al., (2000); Wheatley et al., (2012)), where each ensemble member gets a different set of parameterizations (see Table 2). In particular, the diversity in our ensemble consists of (a) two short- and long-wave radiation schemes [Dudhia (Dudhia, 1989) and RRTMG (Iacono et al., 2008)], (b) three cumulus parameterizations schemes [Kain-Fritsch (KF; Kain and Fritsch, 1993; Kain, 2004), Tiedtke (Tiedtke, 1989) and Grell-Freitas (GF; Grell and Freitas, 2013)] and (c) three planetary boundary layer schemes [Yonsei University (YSU; Hong et al., 2006), Mellor-Yamada-Janjic (MYJ; Janjic, 1990, 2001), and Mellor-Yamada-Nakanishi-Niino level 2.5 (MYNN2; Nakanishi and Niño, 2006, 2009)]. Two widely used physics parameterizations are adopted for the microphysical processes and land surface interactions, the New Thompson (Thompson et al., 2008) and Noah (Tewari et al., 2004) schemes, respectively. Note that the

above-mentioned physical parameterizations are used for both the large-scale ensemble in the parent domain and the storm-scale ensemble in the nested domain, except for the cumulus parameterization that is only applied in the parent domain ensemble. On the other hand, for the WRF deterministic simulation using 3DVar, the microphysical processes are parametrized by using the New Thompson scheme, while a YSU scheme is adopted for PBL. Long- and short-wave radiation are considered through a RRTMG and Dudhia scheme, respectively; while Kain-Fritsch scheme is used for the convection, except for the inner domain where it is explicitly resolved.

Table 2: Multiphysics parameterizations used to generate the 36-member ensemble for the EnKF experiments in IOP13 and Qendresa episodes. PBL, SW and LW stand for planetary boundary layer, short-wave and long-wave, respectively.

Multiphysic Configuration											
Ens. Memb	MP	CU	PBL	Land Sfc	SW/LW Rad.	Ens. Memb	MP	CU	PBL	Land Sfc	SW/LW Rad.
1	New Thompson	KF	YSU	Noah	Dudhia	19	New Thompson	KF	YSU	Noah	Dudhia
2	New Thompson	KF	YSU	Noah	RRTMG	20	New Thompson	KF	YSU	Noah	RRTMG
3	New Thompson	KF	MYJ	Noah	Dudhia	21	New Thompson	KF	MYJ	Noah	Dudhia
4	New Thompson	KF	MYJ	Noah	RRTMG	22	New Thompson	KF	MYJ	Noah	RRTMG
5	New Thompson	KF	MYNN2	Noah	Dudhia	23	New Thompson	KF	MYNN2	Noah	Dudhia
6	New Thompson	KF	MYNN2	Noah	RRTMG	24	New Thompson	KF	MYNN2	Noah	RRTMG
7	New Thompson	GF	YSU	Noah	Dudhia	25	New Thompson	GF	YSU	Noah	Dudhia
8	New Thompson	GF	YSU	Noah	RRTMG	26	New Thompson	GF	YSU	Noah	RRTMG
9	New Thompson	GF	MYJ	Noah	Dudhia	27	New Thompson	GF	MYJ	Noah	Dudhia
10	New Thompson	GF	MYJ	Noah	RRTMG	28	New Thompson	GF	MYJ	Noah	RRTMG
11	New Thompson	GF	MYNN2	Noah	Dudhia	29	New Thompson	GF	MYNN2	Noah	Dudhia
12	New Thompson	GF	MYNN2	Noah	RRTMG	30	New Thompson	GF	MYNN2	Noah	RRTMG
13	New Thompson	Tiedke	YSU	Noah	Dudhia	31	New Thompson	Tiedke	YSU	Noah	Dudhia
14	New Thompson	Tiedke	YSU	Noah	RRTMG	32	New Thompson	Tiedke	YSU	Noah	RRTMG
15	New Thompson	Tiedke	MYJ	Noah	Dudhia	33	New Thompson	Tiedke	MYJ	Noah	Dudhia
16	New Thompson	Tiedke	MYJ	Noah	RRTMG	34	New Thompson	Tiedke	MYJ	Noah	RRTMG
17	New Thompson	Tiedke	MYNN2	Noah	Dudhia	35	New Thompson	Tiedke	MYNN2	Noah	Dudhia
18	New Thompson	Tiedke	MYNN2	Noah	RRTMG	36	New Thompson	Tiedke	MYNN2	Noah	RRTMG

6. Design of IOP13 and Qendresa Experiments

To quantify the benefits of assimilating different observation types with the 3DVar and EnKF DA schemes, a suite of numerical experiments is designed. First, a reference experiment without any data assimilation (NODA), using the same model configuration employed for the

- Eliminado: quantitatively
- Eliminado: assess
- Eliminado: types of
- Eliminado: s
- Eliminado: using
- Eliminado: the
- Eliminado: few
- Eliminado: are performed
- Eliminado: A

WRF experiments performed using 3DVar, is carried out at the regional scales considered in this study. Building on this, several numerical experiments, each differing only in the type of observations assimilated, to isolate and compare their impacts on forecast skill, are performed. Only conventional *in-situ* observations are assimilated using the 3DVar and the EnKF, for the first set of experiments (SYN). All available observations (i.e., conventional, radar based and satellite derived data) are assimilated using both 3DVar and EnKF, for the second type of experiments (CNTRL). The comparison between these numerical experiments will provide information on which DA scheme and observation is performing better for these weather events. The DA experiments mainly consist of two phases: the first one is related to the data assimilation procedure, where different types of observations are assimilated by the variational 3DVar and the ensemble-based EnKF DA schemes; the second phase is associated with the free model run initialized using the initial conditions obtained during the first phase. The total forecast time is 24 h and 36 h for IOP13 and Qendresa, respectively. For IOP13, a further simulation lasting 6-hour from 18 UTC 13 October to 00 UTC 14 October 2012 (Carrió et al., 2019) is performed (Fig. 6) to reduce spin-up problems related to the direct downscaling from global ECMWF analysis (32 km grid resolution) to the WRF parent domain used in our simulations (16 km grid resolution). This procedure improved the DA for IOP13, but it had a small impact for Qendresa.

Therefore, the following model simulations were performed:

- No Data Assimilation (NODA)
- Only conventional *in-situ* observations are assimilated using the 3DVar and the EnKF (SYN)
- All available observations (i.e., conventional, radar based and satellite derived data) are assimilated using both 3DVar and EnKF (CNTRL)

The comparison between the DA experiments and NODA allows us to assess the impact of the DA procedure. On the other hand, the comparison between SYN and CNTRL will allow for assessing the role of radar and/or satellite data, especially for the events originated in the area where observations are not available. Moreover, the assimilation of the radar and/or satellite will produce important information on the triggering phase of both events developing on the sea.

6.1. CNTRL Experiments

For IOP13, the CNTRL experiment is designed to assimilate both *in-situ* conventional and reflectivity observations from Aleria and Nimes Doppler weather radars. The assimilation of the reflectivity is expected to improve the forecast of this event by significantly improving the initial conditions over the sea, where convective activity initiated and evolved into deep convection affecting coastal populated areas of Italy. As briefly described in the previous section, this experiment consists of three stages: 1) the spin-up of the storm-scale domain is accounted for by running the WRF model during 6 hours from 18 UTC 13 October to 00 UTC 14 October 2012 (note that for the 3DVar experiment, the spin-up is accounted for by just initializing WRF with the deterministic analysis from the IFS ECMWF. However, for the EnKF counterpart, the spin-up is accounted by initializing the 36-member ensemble at 18 UTC 13 October); 2) *in-situ* conventional observations were hourly assimilated during 24 hours from 00 UTC 14 October to 00 UTC 15 October, meanwhile reflectivity observations were

Eliminado:

Eliminado: is carried out

Eliminado: Then,

Eliminado: using

Eliminado: variations of the NODA but now assimilating

Eliminado: different types of observations for the assimilation are performed

assimilated using a Rapid-Update Assimilation Cycle every 15 minutes during a period of 6 hours, from 18 UTC 14 October to 00 UTC 15 October (Fig. 6); 3) a 24-h ensemble (deterministic) forecast until 00 UTC 16 October, using the recently obtained initial conditions, is performed by the EnKF (3DVar).

For the Qendresa episode, CNTRL experiment is designed to assimilate both *in-situ* conventional and RSAMV observations. The assimilation of RSAMV observations is expected to improve the representation of the atmospheric circulation at upper-levels, whereas the assimilation of surface conventional observations is expected to enhance the one at low-levels. The Qendresa CNTRL experiment consists of two main phases: 1) *in-situ* conventional and satellite derived RSAMV observations are hourly and 20-min assimilated, respectively, during a 12-h period from 12 UTC 6 November to 00 UTC 7 November 2014 to end up with the last analysis at the end of the assimilation window (i.e., 00 UTC 7 November); 2) a free 36-h ensemble (deterministic) forecast is performed by the EnKF (3DVar) from 00 UTC 7 November to 12 UTC 8 November 2014 (Fig. 6e).

6.2. SYN Experiments

For IOP13, the SYN experiment assesses the impact of *in-situ* conventional observations, which are crucial to characterize mesoscale atmospheric circulation. Analogous to the CNTRL, SYN follows the same three phases, but in the second phase only the hourly *in-situ* conventional observations from 00 UTC 14 October to 00 UTC 15 October 2012 are assimilated. The analysis obtained from the assimilation stage is used as initial conditions for running the free forecast for 24h, in the third phase (Fig. 6).

Similarly, also for Qendresa, in the SYN experiment only *in-situ* conventional observations are hourly assimilated for 12 hours, from 12 UTC 6 November to 00 UTC 7 November 2014 (Fig. 6).

6.3. NODA Experiments

For the IOP13, NODA experiment is a direct downscaling from EPS-ECMWF boundary and initial conditions valid at 18 UTC 13 October to 00 UTC 16 October 2012 (Fig. 6). The comparison among NODA, CNTRL and SYN will provide us with valuable information on the impact of assimilating different sources of observations.

For Qendresa, NODA experiment is simply a direct downscaling of 36 hours from EPS-ECMWF at 00 UTC 7 November to 12 UTC 8 November 2014 (Fig. 6). Here again, it is important to note that the choice of starting NODA at 00 UTC 7 November instead of starting at 12 UTC 6 November was made intentionally to extract general conclusions applicable possibly to an operational framework.

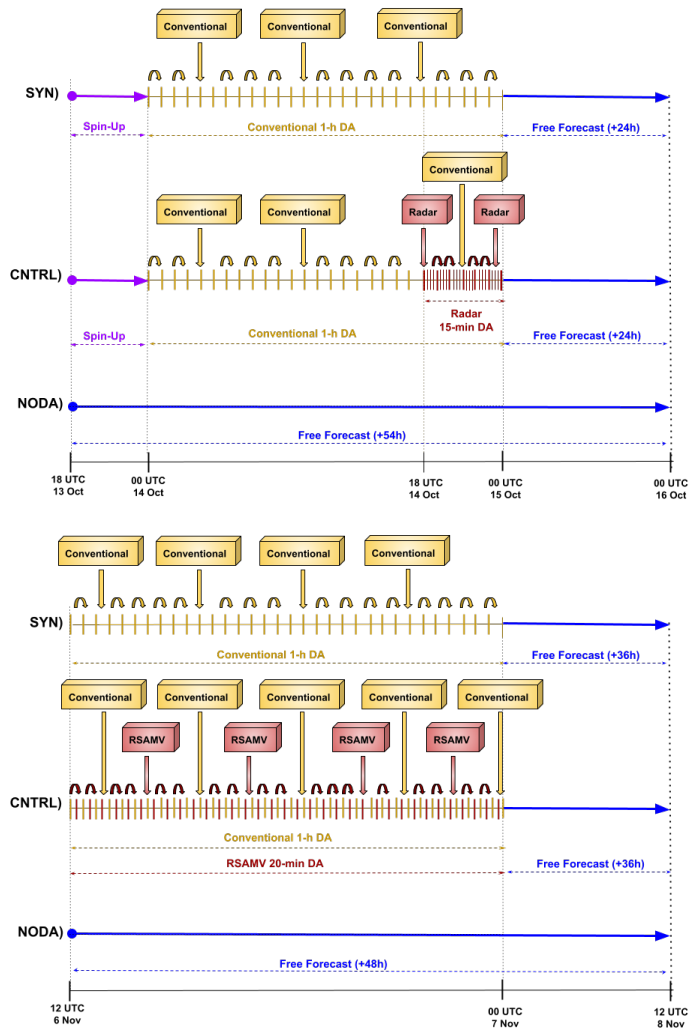
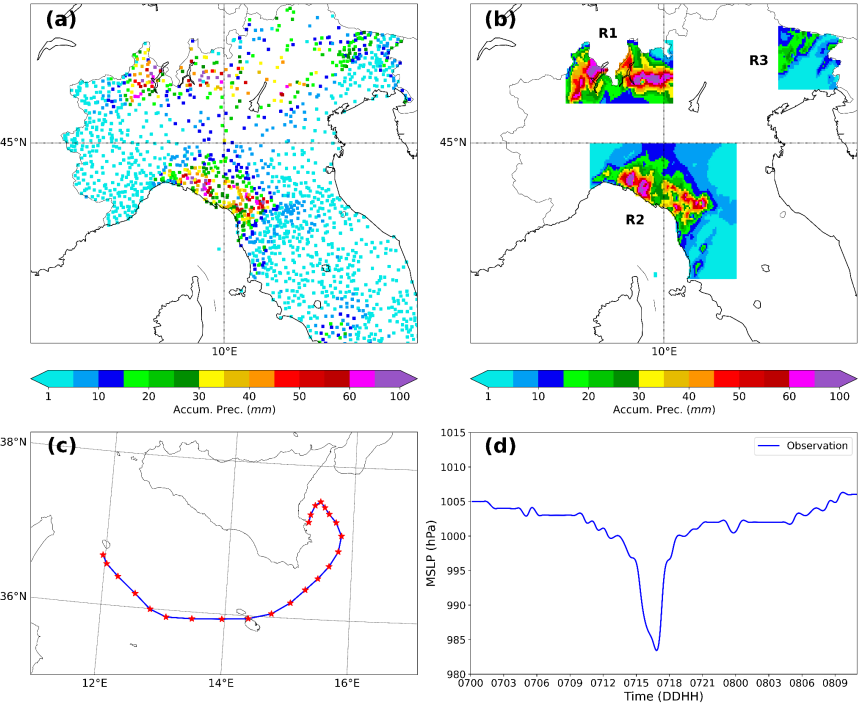


Figure 6. Schematic representation of the main numerical experiments performed in this study for the IOP13 (top panel) and Qendresa (bottom panel) episodes, respectively. SYN, CNTRL and NODA experiments are illustrated for each case, highlighting their respective configurations and assimilation strategies.

7. Verification Methods

To quantitatively evaluate the performance of the EnKF and the 3DVar and their impact on the short-term forecast of these two extreme weather events, various verification scores are used. Given the different nature of the weather phenomena associated with these episodes, the selection of verification scores is tailored specifically to each event. For the IOP13 heavy precipitation event (Fig. 7a), the model verification was performed using the observed accumulated precipitation field over different time windows (e.g., 3 hours, 6 hours or 9 hours).

758 More specifically, the accumulated precipitation was computed using observations from the
 759 *Italian Department of Civil Protection*. However, the spatial distribution of rain gauges is not
 760 homogenous and there are regions where a lack of rain gauges is present. To address these
 761 issues, three sub-regions are chosen where the heavy precipitation event was well recorded by
 762 the weather stations (see R1, R2 and R3 in Fig. 7b). Conversely, for the Qendresa tropical-like
 763 cyclone, a limited number of *in-situ* observations were present since it initiated and moved over
 764 the sea during its lifecycle, and radar-data were not available. Consequently, IR satellite
 765 imagery was the primary source of data to approximately estimate Qendresa's trajectory (Fig.
 766 7c). Regarding the intensity of Qendresa, since the cyclone's center passed over Malta island,
 767 reaching its minimum mean sea level pressure (MSLP) of 985 hPa, METAR data from Malta's
 768 airport was also used to verify the cyclone's intensity (Fig. 7d).
 769



770 **Figure 7.** (a) Example of the 12-h accumulated precipitation estimated values and their spatial distribution from
 771 the Italian Department of Civil Protection rain gauges. (b) Linear interpolation of 12-h accumulated precipitation
 772 values into the three target areas where verification has been performed. (c) Observed track of Qendresa
 773 medicane viewed from infrared satellite imagery. (d) Surface pressure (hPa) data obtained from the METAR
 774 station at Malta's airport.
 775
 776
 777

778 To quantitatively assess the short-term (i.e., first 6-9 hours) precipitation forecast for the IOP13
 779 initialized using the analysis from the 3DVar and EnKF DA techniques, the *Filtering Method*,
 780 the *Relative Operating Characteristics* (ROC; Mason, 1982; Stanski et al., 1989; Swets, 1973)
 781 and the *Taylor Diagrams* (Taylor, 2001) were used. We avoid using the conventional point-
 782 by-point approach, which has been shown to have serious limitations in the evaluation of high-

grid spatial and temporal precipitation field resolutions (Roberts, 2003). More specifically, as *Filtering Method* we use the *Fraction Skill Score* (FSS; Roberts and Lean, 2008), which is commonly used to quantitatively assess precipitation. A preliminary interpolation of the forecast and the observations onto a common regular mesh of 3 km is performed to compute FSS. Then the comparison is carried out within a region of 3x3 grid cells around each grid cell. The FSS can be used to determine the scale over which a forecast system has sufficient skill (Mittermaier, 2010). The FSS ranges from 0 to 1, being 1 a perfect match between model and observations. In addition to the ROC curves, the *Area Under the ROC Curve* (AUC; Stanski et al., 1989; Schwartz et al., 2010), which is also widely used to quantitatively assess the quality of weather forecasts, will be also used in this study. For a perfect forecast, AUC is equal to 1.

For Qendresa, the *Whisker diagrams* (Tukey, 1977) and the *Probability Distribution of the Cyclone Center Occurrence* (**PCCO**), which was based on the *Kernel Density Estimation* (KDE; Bowman and Azzalini, 1997; Scott, 2015; Silverman, 2018), were used to validate the simulations. More specifically, the KDE is used to compute the probability of having the center of the cyclone over the entire numerical domain. The main idea behind KDE is to place a “kernel” (i.e., a probability distribution function) at each data point, and then sum up the kernels to estimate the overall probability density function. The kernel is typically chosen to be a smooth function, such as a Gaussian, that decays to zero as the distance from the data point increases. The width of the kernel is controlled by a parameter called the bandwidth, which it turns out to be one of the limitations of the KDE technique. In this case, we found that the optimal bandwidth is 20 km, which is within the meso β scale, i.e. a typical length scale for convective cells. Here, a 2-dimensional KDE will be applied over each cyclone center (*lat, lon* coordinates) identified for the different simulations (i.e., EnKF vs 3DVar). In this way, we will infer the most probable track of Qendresa for the different simulations, thereby identifying which is the best DA technique and which provides better estimations of Qendresa medicane’s track.

8. Results

As discussed in the previous section the above-mentioned verification techniques were applied for the two extreme events. The results are described in the following subsections.

8.1. Statistical analysis: IOP13 Episode

Because IOP13 was a heavy rainfall episode, to quantitatively assess the impact on the short-range forecasts from assimilating both *in-situ* conventional and reflectivity observations from Doppler weather radars using the 3DVar and the EnKF DA algorithms, the accumulated precipitation field will be used.

8.1.1. Filtering Method

The FSS associated with the 3-h accumulated precipitation field is computed independently for the three sub-regions R1, R2 and R3, which are highlighted in Fig. 7b. These regions were chosen due to their higher observation density, allowing for a more reliable evaluation. The analysis is carried out using two precipitation thresholds: 5 mm·h⁻¹ (moderate rainfall) and 10 mm·h⁻¹ (heavy rainfall). In general, except for R3, the comparison in terms of FSS (Fig. 8 a-f)

shows that at the initial forecast time and during the first 6 hours, DA simulations (EnKF and 3DVar) outperform the NODA simulation (without assimilation). Among the DA simulation, EnKF generally outperforms 3DVar in R1 and R2, especially for the higher precipitation threshold ($10 \text{ mm} \cdot \text{h}^{-1}$). As expected, CNTRL experiments for both 3DVar and EnKF provide higher FSS values compared to SYN experiments, where reflectivity observations were not considered.

In R3, the results show an unexpected behavior when using the moderate threshold ($5 \text{ mm} \cdot \text{h}^{-1}$) (Fig. 8c), where NODA outperforms DA simulations during the first few hours. This anomaly could be attributed to three factors: (1) the use of a moderate precipitation threshold, which may not capture significant precipitation differences; (2) minimal precipitation in R3 during the initial forecast hours, since the deep convection system had not yet reached this region; and (3) the location of R3 near the domain edges, where it relies solely on in-situ observations for assimilation corrections, as it falls outside the radar coverage area. This interpretation is reinforced when examining the higher precipitation threshold ($10 \text{ mm} \cdot \text{h}^{-1}$) (Fig. 8f), where all methods exhibit similarly poor skill in the early forecast hours, indicating that precipitation is still too weak to be meaningfully assessed. However, after 6-9 hours, as expected, DA simulations outperform NODA in all sub-regions.

To be noticed, the CNTRL simulations do not consistently show better FSS scores than SYN simulations during the first hours, for R1. This could be due to the short-lived impact of radar reflectivity assimilation, which in past studies has been shown to last no longer than 2-4 hours for 3DVar and EnKF, respectively. These findings align with previous studies, which reported similar behavior regarding the transient impact of reflectivity DA (Carrió et al., 2016; Carrió et al., 2019).

Finally, we also computed the Root Mean Squared Error (RMSE) for the precipitation field over the first 24 hours of free forecast for both DA and NODA experiments (Fig. 8g-i). For 3DVar and NODA, RMSE is calculated from the deterministic forecast, while for EnKF, it is computed from the ensemble mean precipitation field. Overall, DA experiments exhibit lower (better) RMSE scores compared to NODA, confirming the positive impact of data assimilation on forecast accuracy. Among the DA experiments, EnKF consistently outperforms 3DVar in all regions, suggesting a better representation of precipitation variability and improved initial conditions.

Eliminado: In R3, the results show an unexpected behavior when using the moderate threshold ($5 \text{ mm} \cdot \text{h}^{-1}$) (Fig. 8c), where NODA outperforms DA simulations during the first few hours. This anomaly could be

Eliminado: attributed

Eliminado: explained by

Eliminado: to

Eliminado: two

Eliminado: three

Eliminado: factors: (1) the

Eliminado: use of a

Eliminado: moderate precipitation threshold, which may not capture significant precipitation differences

Eliminado: ;

Eliminado: , and (2) the fact that in the first few hours,

Eliminado: minimal

Eliminado: precipitation in R3

Eliminado: during the initial forecast hours,

Eliminado: is minimal since the deep convection system

Eliminado: had

Eliminado: has not yet reached this region.

Eliminado: ; and (3) the location of R3 near the domain edges, where it relies solely on in-situ observations for assimilation, as it falls outside the radar coverage area.

Eliminado:

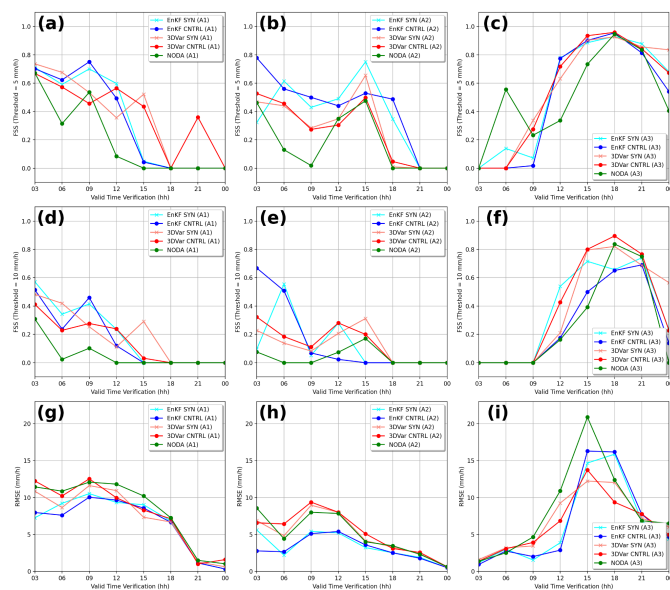
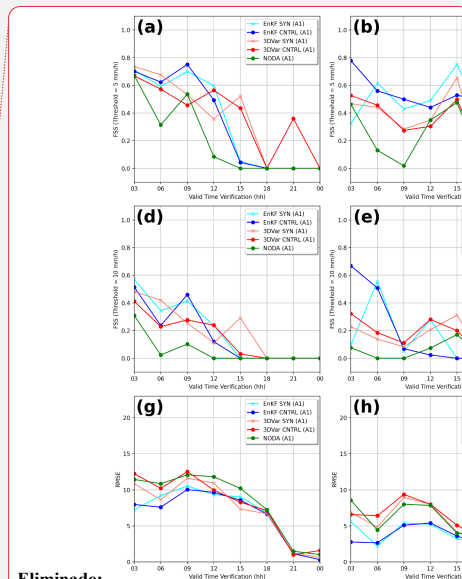


Figure 8. Upper panels: Evolution of the FSS during the first 24-h hours of free forecasts for 3-h accumulated precipitation in the Italian sub-regions: R1 (first column), R2 (second column) and R3 (third column). Two thresholds are used: $> 5 \text{ mm}\cdot\text{h}^{-1}$ (first row) and $> 10 \text{ mm}\cdot\text{h}^{-1}$ (second row). Lower panels: Evolution of the RMSE associated with each experiment during the first 24 hours of free forecast in the different sub-regions. Simulations assimilating both conventional and radar observations (CNTRL) and simulations assimilating only conventional observations (SYN) associated with the 3DVar and the EnKF are shown here. As a reference, NODA results are also included.

8.1.2. ROC and AUC

To strengthen how skillful are the different simulations performed by the 3DVar and the EnKF, the *Receiver Operating Characteristic* (ROC) curve is used. The probability of exceeding a given threshold is computed and verified against dichotomous observations. The ROC curve is computed as follows: the model variable is interpolated to the observation locations and if the model variable exceeds a given threshold, that model grid point is assigned a value of 1. On the contrary, if the model value does not exceed that threshold, the assigned value is 0. The same method is applied for the observations. Then, using these dichotomous values, the *Hit Rate* and *False Alarm* scores are computed. This process is repeated, varying the threshold value. Gathering the *Hit Rate* and *False Alarm* scores for the different thresholds, we obtain the ROC curve. For the 3DVar, we get the *Hit Rate* and *False Alarm* scores by simply interpolating the model values to the observation locations and apply the threshold criteria explained above. In the case of the EnKF, the ensemble mean is used as the field to be interpolated to the observation locations. The area under the ROC curve (AUC), which measures the ability of the system to discriminate between the occurrence or nonoccurrence of the event, is also computed.

For the sake of brevity and because the results from the three sub-regions are similar, the ROC curve and AUC are computed, accounting for all the observations within the inner domain.



Eliminato:

Specifically, to compute the ROC curves, we use the 3-hour (from 00 UTC - 03 UTC 15 Oct) and 6-hour (from 00 UTC - 06 UTC 15 Oct) accumulated precipitation fields from the model simulation and the observed values registered by the rain gauges, using 1 mm and 10 mm as thresholds (Fig. 9).

Overall, DA experiments outperform the NODA runs for both the 3-hour and 6-hour accumulated precipitations, as shown by higher ROC curves and larger AUC values. Among the DA approaches, the EnKF consistently outperforms 3DVar, with greater benefits observed at the 10 mm threshold (i.e., bottom row of Fig. 9). This improvement highlights the advantages of radar reflectivity assimilation within an ensemble-based framework, especially for more intense precipitation events. To better understand this result, we closely analysed the 1-h and 6-h accumulated precipitation fields obtained from the EnKF (CNTRL) and the 3DVar (CNTRL) comparing them against corresponding observations (see Fig. A1 and Fig. A2 in the Appendix). The 1-h accumulated precipitation (Fig. A1) shows that the EnKF localizes with high accuracy the regions where the most intense precipitation was observed, that is near Tuscany and northern Italy. Also, 3DVar correctly reproduces the rainfall in the regions affected by observed precipitation, although the maximum amounts are centered over Liguria, instead of near Tuscany. In addition, the 3DVar is also showing a tongue area of weak precipitation from Liguria to northern Italy, that does not fit with the observations. Consequently, while small differences exist between 3DVar and EnKF in the 1-h accumulated precipitation field, the low magnitude of accumulated precipitation values leads to no substantial differences in ROC verification scores. However, in the case of the 6-h accumulated precipitation (Fig. A2), the 3DVar overestimates accumulated precipitation near Liguria, Tuscany and northern Italy than the observed ones. Moreover, 3DVar is also misplacing the locations of the precipitation for some places. On the contrary, the EnKF locates with enough accuracy the regions where the accumulated precipitation was actually observed and properly estimates the observed intensity. Consequently, ROC curve for the 6-hour accumulated precipitation obtained from the EnKF produced a much better score than the 3DVar. We hypothesize that this difference could be associated with the *static/climatological* background error covariance matrix used by the 3DVar. Because of the fast changes in the flow associated with the IOP13 case, using a climatological background error covariance could not be as good as using a flow-dependent background error covariance matrix, which is used in the EnKF.

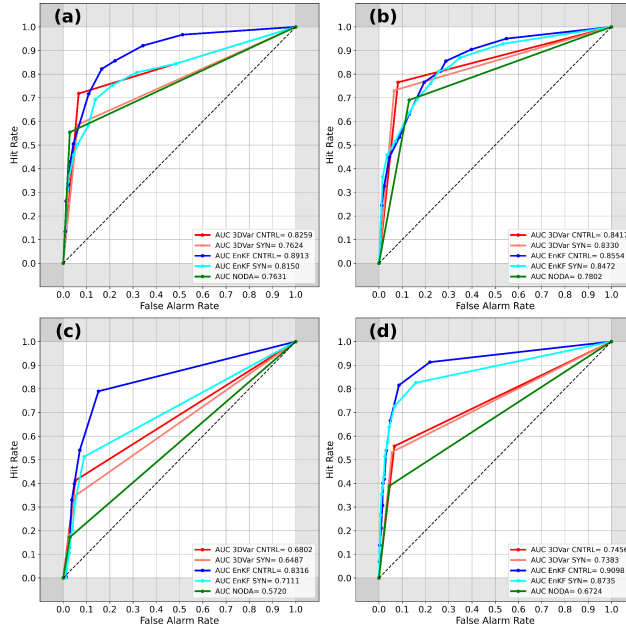


Figure 9. ROC curves and AUC associated with the 3DVar (red and pink colors), EnKF (blue and cyan colors) and NODA (green color) for the 3-hour accumulated precipitation using (a) 1 mm and (b) 10 mm threshold and 6-hour accumulated precipitation using (c) 1 mm and (d) 10 mm threshold, computed over the entire inner domain. *Note: all experiments employ the same set of probability thresholds; any apparent differences in the number of plotted points arise from clustering of ROC values at similar thresholds, not from differing data counts.*

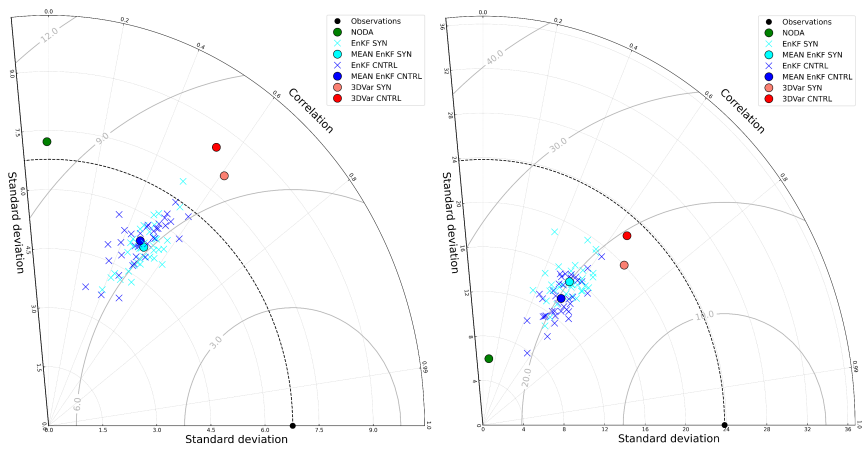
Eliminado: ROC curves and AUC associated with the 3DVar (red and pink colors), EnKF (blue and cyan colors) and NODA (green color) for the 3-hour accumulated precipitation using (a) 1 mm and (b) 10 mm threshold and 6-hour accumulated precipitation using (c) 1 mm and (d) 10 mm threshold, computed over the entire inner domain.

8.1.3. Taylor Diagrams

To strengthen the comparison of the DA schemes, the Taylor Diagram is used. This tool provides us additional information about the skill of each ensemble member in the EnKF. Here, we compute the Taylor diagram for the 6-hour and 24-hour accumulated precipitation fields, which represents the forecast ranges where the observations assimilated have more impact. Overall, results show that the NODA experiment generally exhibits the lowest correlation and largest discrepancy in standard deviation relative to observations, emphasizing that DA significantly improves the representation of precipitation fields, especially for high-impact weather events. Among the different DA approaches, the 3DVar and the EnKF ensemble mean provide comparable results, with correlations ranging from approximately 0.50 to 0.61, similar RMSE and standard deviation that are symmetrically distributed around the observed reference. Notably, 3DVar tends to overestimate the standard deviation, while the EnKF ensemble mean tends to underestimate it (Fig. 10). A key advantage of EnKF lies in its individual ensemble members, some of which exhibit better performance than the 3DVar run. Although the mean difference between EnKF and 3DVar is small, the ensemble-based approach provides additional insight through its member-by-member variability. Specifically, ensemble members using the Grell-Freitas cumulus parameterization coupled with the Yonsei University planetary boundary layer scheme exhibit higher correlation and standard deviations similar to the observations in this study. Conversely, ensemble members associated with the lower scores are those using Kain-Fritsch for the cumulus parameterization and the Mellor-

991 Yamada-Janjic for the planetary boundary layer scheme. These findings underscore the
992 potential of multi-physics ensembles to capture diverse physical representations of convective
993 processes, thereby enhancing forecast accuracy.

994



995

996 **Figure 10.** Taylor diagram comparing the performance of 3DVar (red), EnKF (blue) and NODA (green) for the
997 6-hour (left panel) and 24-hour (right panel) accumulated precipitation, valid at 06 UTC 15 October 2012.

998

999

1000 **8.2. Statistical analysis: Qendresa event**

1001

1002 In tropical cyclone forecasting, two key factors are typically evaluated: (a) the intensity and (b)
1003 the trajectory followed by the cyclone. Therefore, to assess the impact of assimilating both *in-*
1004 *situ* conventional and remote RSAMV observations using the 3DVar and the EnKF, we focus
1005 on these two factors for the Qendresa event.

1006

1007

1008 **8.2.1. Whisker Diagrams**

1009

1010 For this event, the lack of *in-situ* observations over maritime regions poses a main challenge to
1011 properly verify the triggering and intensification of cyclones. Fortunately, the Qendresa
1012 medicane crossed just over Malta island, where a pressure drop greater than 20 hPa in 6 h, was
1013 registered by METAR at Malta airport, reaching a minimum of surface pressure of 985 hPa.
1014 Therefore, this METAR is used to quantitatively assess the skill of the NODA simulation and
1015 the various DA approaches. To compare the surface pressure registered at Malta with the
1016 different simulations, the full cyclone trajectory is used, and the grid point closest to Malta
1017 airport is selected. Specifically, the surface pressure time series measured by METAR is
1018 compared with the NODA run and the different DA simulations from 3DVar and EnKF, such
1019 as the 3DVar_SYN, 3DVar_CNTRL, EnKF_SYN, and the EnKF_CNTRL (Fig. 11).

1020

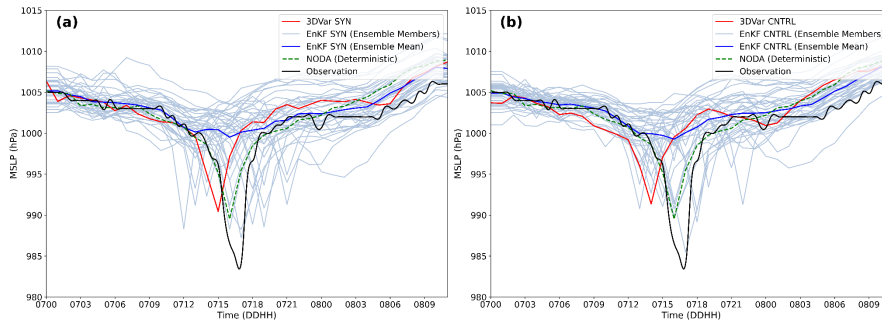


Figure 11. Temporal surface pressure evolution at the closes grid point to Malta for the (a) SYN and (b) CNTRL experiments associated with the EnKF (blue), 3DVar (red) and NODA (green), compared to the observed surface pressure registered by METARs in Malta's airport (black line).

Overall, results indicate that NODA simulation captures the timing of the observed pressure drop more accurately than the DA runs, suggesting that the large-scale dynamics are adequately represented even without data assimilation (Fig. 11). However, NODA underestimates the intensity of the medicane's central pressure.

Among the DA simulations, assimilating *in-situ* conventional observations enables some EnKF ensemble members to outperform NODA in both timing and intensity, whereas 3DVar shows limitations in capturing the event timing and central pressure depth (Fig. 11a). Additionally, the ensemble mean of the EnKF_SYN accurately fits the observations during the first hours of the forecast, from 00 UTC to 13 UTC 7 November (Fig. 11a), performing slightly better than 3DVAR_SYN. However, during the intensification phase, the ensemble mean of the EnKF_SYN barely shows the intensification of Qendresa, reaching minimum MSLP values of 1002 hPa. On the contrary, the 3DVar_SYN simulation depicts the intensification of the medicane, by deepening the MSLP and reaching values of 992 hPa, although a time shift of 3 hours is found (i.e., 15 UTC 7 November) (Fig. 11a). Finally, during the dissipation phase of Qendresa, the ensemble mean of EnKF_SYN is performing a bit better than the 3DVar_SYN (Fig. 11a). These results highlight a notable limitation of the EnKF when applied to low-predictable weather events, such as Qendresa. The low predictability of Qendresa and the high sensitivity to physical parameterizations produce substantial spread in ensemble behavior: some members capture the cyclone's closed circulation and track reasonably well, while others fail to develop a coherent low-pressure core, instead producing only disorganized or weak convective cells. Consequently, these poorly performing members may entirely miss the medicane's formation or misplace its center, leading to large errors in both track and intensity forecasts. In this situation, our small-to-moderate ensemble size exacerbates sampling error, yielding spurious background error covariances that degrade analysis accuracy in the EnKF. These errors become particularly problematic when the numerical model mispredicts the event, since the ensemble members no longer provide a reliable representation of flow-dependent uncertainty. On the other hand, a climatological/static background error covariance matrix, like the one used in the 3DVar could produce better results than ensemble members, as we see in Fig. 11a where we compared the 3DVar (red line) with the EnKF ensemble mean analysis (blue line). Also, it is important to note that although the ensemble mean of the EnKF_SYN is not correctly reproducing the intensification of Qendresa, some of the ensemble members very well reproduce the observed MSLP both in deepening and timing. This suggests that using an ensemble system, even having the above-mentioned problems, is still more useful than using

Eliminado: The low predictability and the high sensitivity to the different physical parameterization schemes lead to a very different behavior of each ensemble member. Consequently, some members could completely fail in the prediction of the weather event.

Eliminado: will probably produce a poor flow-dependent background error covariance matrix, which is key in DA, resulting in an analysis ensemble with large spread, for which the ensemble mean will be smoothed out significantly.

only a fully deterministic system such as the 3DVar, which cannot provide information about the uncertainties of the system. Therefore, we can speculate that for extreme weather events with low numerical predictability, a better approach could be using a hybrid error covariance model, where the forecast error covariance matrix is obtained linearly combining ensemble-based covariance with static climatological error covariances (Hamill and Snyder (2000); Lorenc (2003); Clayton et al., 2013; Carrió et al., 2021). The impact of using hybrid DA to improve this kind of small-scale extreme weather events could be of great interest in the weather forecast community, although it is beyond the scope of this study. For this reason, the authors leave as future work the benefits of using hybrid error covariance models to improve the forecast of extreme weather events in the Mediterranean basin.

Then, we evaluated the impact of assimilating both *in-situ* conventional and RSAMV observations on the accuracy of Qendresa intensity forecast (Fig. 11b). In this case, the results of the two experiments show large similarities (Fig. 11a,b). In terms of the 3DVar, the MSLP signature is basically the same, without showing a clear signal of improvement or diminishing, suggesting that the assimilation of RSAMVs is not enough to significantly improve the low level relevant dynamical structures associated with the genesis and intensification of Qendresa. However, in terms of the EnKF a clear improvement for a few members is found, even if it is not affecting the mean value. Indeed, some of the ensemble members depicted an intense cyclone far from the time when it was observed (approx. at 18 UTC 7 November), were corrected reducing spurious cyclones and the deepening of at least one ensemble member close to the observed value (Fig. 11b). It can be observed that in the EnKF_CNTRL, there are more ensemble members depicting a deep cyclone at the observed time than in the case of the EnKF_SYN, showing the benefits of assimilating RSAMVs to improve the intensification estimation of Qendresa.

To quantitatively assess the performance of NODA and the different DA experiments, we use the lagged correlation technique computed between the model MSLP signatures and the observations. This technique allows us to measure how the shape of the surface pressure evolution obtained from the different simulations fits the shape of the observed MSLP, taking also into account temporal shifting. The correlation is computed for the NODA, 3DVar, and for each ensemble member from the EnKF. These results are shown using Whisker plots (Fig. 12), where a correlation of one indicates that the specific model field has the same ‘V’ pressure shape evolution as the observation, and that the minimum for both is found at the same time. The results show that the NODA simulation exhibits the highest correlation values among all the simulations, reaching its maximum correlation when no time-shifting is applied. For the 3DVar_SYN, the correlation is maximum and approximately equal to one when a 1-hour delay is produced by the forecasts (Fig. 12a). Whiskers from EnKF_SYN show that none of the ensemble members overcomes the maximum correlation value found in 3DVar_SYN. However, when the assimilation of RSAMVs is added to the *in-situ* conventional observations, it is found that the maximum correlation value associated with 3DVar_CNTRL using 2h of delay applied to the forecasts, is surpassed by some of the ensemble members of the EnKF_CNTRL, when a 3 or 4 hour of delay is applied (Fig. 12b).

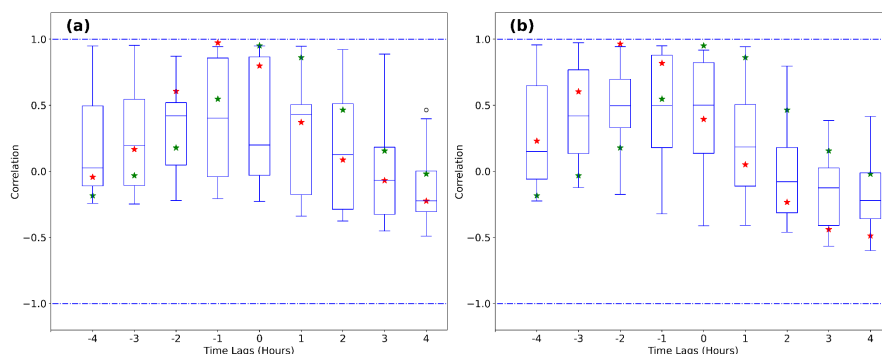


Figure 12. Whisker plots depict the lagged correlation values between the observations and the EnKF (blue boxes), the 3DVar (red stars) and NODA (green stars) for the (a) SYN and (b) CNTRL experiments. The correlation is computed considering that the observed V-shape pressure signature associated with the observations is shifted 4 hours to the left and 4 hours to the right.

8.2.2. Probability Distribution of Cyclone Center Occurrence

Due to the difficulty to accurately predict the observed trajectory of Qendresa (Pytharoulis et al., 2018), the impact of assimilating different kinds of observations on the trajectory of the medicane is investigated.

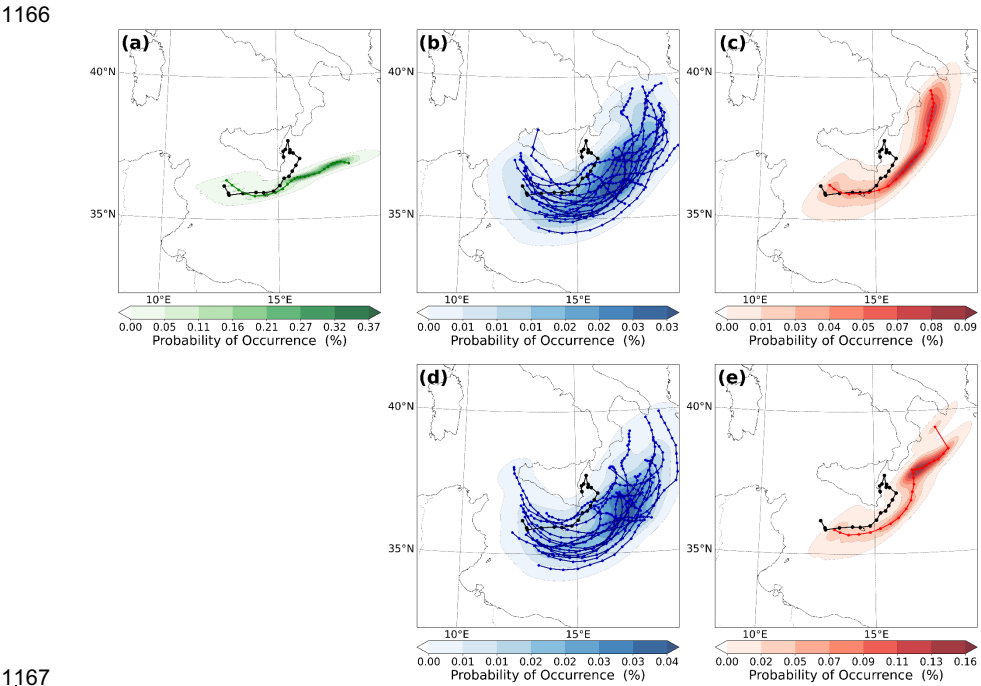
Results indicate that the NODA simulation fails to accurately capture the track of Qendresa, especially its recurvature towards Sicily after leaving Malta, as evidenced by satellite imagery. In contrast, the 3DVar_SYN accurately captures the track of Qendresa during the first hours (Fig. 13b). However, after Qendresa leaves Malta, the trajectory simulated by 3DVar_SYN diverges from the observed track, shifting north-eastwards and failing to capture the track-loop observed in satellite imagery. To quantify the benefits of assimilating *in-situ* conventional observations using the 3DVar or the EnKF, the probability of occurrence of a cyclone following the track observed via satellite imagery is computed. For instance, 3DVar_SYN underestimates the probability of cyclone occurrence east of Sicily, where Qendresa made landfall while looping (Fig. 13b). On the other hand, some EnKF_SYN ensemble members show a cyclone trajectory shifted significantly southward, while others reproduce the loop trajectory missed by the NODA forecast (Fig. 13a). In addition, the probability of Qendresa occurrence eastwards Sicily, is in this case larger than 3DVar_SYN, showing the benefits of using the EnKF against the 3DVar (Fig. 13a). Moreover, the EnKF_SYN ensemble trajectories, in general, follow a ‘V’ shape (i.e., first moving towards the southeast, then moving to the east and finally moving towards the northeast) similar to the trajectory observed via satellite imagery. Although the shape of most of the EnKF_SYN trajectories agree with the observations, a consistent southeastward displacement is evident in their location.

If both *in-situ* conventional and RSAMV observations are assimilated, some of the ensemble members from the EnKF_CNTRL shows more accurate trajectories in comparison with EnKF_SYN: the loop trajectory is closer to the observed region of eastern Sicily (Fig. 13c). An improvement of the 3DVar_CNTRL trajectory by increasing the probability of cyclone occurrence following the observed track is observed, especially eastern of Sicily. However, 3DVar experiments are not able to reproduce the looping trajectory observed via satellite imagery (Fig. 13b-d). Hence, EnKF outperforms 3DVar showing some of the ensemble

Eliminado: deterministic numerical weather models

1154 members depicting a loop trajectory, although shifted southwards and producing a probability
1155 of cyclone occurrence lower than the 3DVAR ones.

1156 Both the EnKF and the 3DVar still have difficulties in depicting accurately the track observed
1157 by Qendresa, even after the assimilation of *in-situ* conventional and RSAMV observations.
1158 Because RSAMVs are useful in describing dynamical features on the upper levels of the
1159 atmosphere, we hypothesize that ingesting them via DA may not be sufficient to correct key
1160 low-level dynamical features. In this case, the assimilation of surface wind observations may
1161 help to even improve these results. However, this is beyond the scope of this study and the
1162 authors leave this question as future work, where other sources of information from satellites
1163 will be assimilated to improve low-level thermodynamic aspects of extreme weather events,
1164 such as medicanes.



1167
1168 **Figure 13.** Probability of cyclone center occurrence (*within 20 km*) computed using Gaussian KDE for (a) NODA,
1169 (b) EnKF (SYN), (c) 3DVar (SYN), (d) EnKF (CNTRL) and (e) 3DVar (CNTRL), from 11 UTC 7 November to 12
1170 UTC 8 November 2014. Qendresa's trajectory observed via satellite imagery is depicted in black.

1171
1172
1173 **9. Summary and Conclusions**

1174
1175 This study provides a quantitative assessment of the impact of two widely used DA techniques
1176 – 3DVar and EnKF – on the predictability of maritime extreme weather events. The focus is
1177 on evaluating their potential to improve forecast lead time by assimilating observations during
1178 the developing stage, as opposed to the mature stage, which affords limited time for
1179 preparedness and response. To evaluate the performance of 3DVar and EnKF, we analyze two
1180 high-impact weather events triggered over the sea and later affected densely populated coastal

1181 regions. These two extreme weather events are known as (a) the high precipitation event
1182 registered during the 13th Intensive Observation Period (IOP13) affecting the western, northern
1183 and central parts of Italy, and (b) the intense Tropical-like Mediterranean Cyclone (medicane)
1184 known as Qendresa, that affected the islands of Pantelleria, Lampedusa, Malta and Sicily.
1185 These weather events pose a serious challenge for the numerical weather prediction community
1186 due to their low predictability, resulting from their initialization over the sea, where *in-situ*
1187 observations are sparse and initial conditions are poorly estimated. Furthermore, their evolution
1188 over complex terrain regions introduces additional forecasting challenges.

1189
1190 For these two extreme weather events, both 3DVar and EnKF DA methods were applied, with
1191 the type and number of assimilated observations varying based on the data availability. For
1192 Qendresa, we assimilated (a) hourly *in-situ* conventional observations and (b) wind speed and
1193 wind direction profiles of the entire atmosphere (RSAMVs) derived from geostationary
1194 satellites every 20-min, providing high spatial and temporal resolution observations covering
1195 the Central Mediterranean Sea, where Qendresa initiated and evolved. On the other hand, for
1196 the IOP13, we assimilated (a) hourly *in-situ* conventional observations and (b) 15-min 3D
1197 reflectivity observations from two type-C Doppler Weather Radars.

1198
1199 Because of the different thermodynamic characteristics associated with Qendresa and IOP13,
1200 a set of different verification metrics were used for each of these extreme weather events. The
1201 *Filtering* method (FSS and RMSE), the ROC/AUC and the Taylor diagram were used to verify
1202 the numerical simulations from 3DVar and EnKF associated with IOP13. In the case of
1203 Qendresa, we used the Whisker diagrams and the Probability Distribution of Cyclone Center
1204 Occurrence verification scores. For the IOP13, both the *Filtering* method and Taylor diagram
1205 verification show that EnKF slightly outperforms 3DVar, although the differences are not
1206 significant. In addition, it was observed that the assimilation of spatial and temporal high-
1207 resolution reflectivity observations significantly improved the forecast for both 3DVar and
1208 EnKF, showing the key role of this type of observation. On the other hand, the ROC and AUC
1209 scores clearly show that EnKF outperforms 3DVar. For the Qendresa event, while the ensemble
1210 mean of EnKF underestimates the intensity of the medicane compared to 3DVar, some
1211 individual EnKF ensemble members produce more accurate results than 3DVar. This
1212 behaviour suggests how important it is using an ensemble forecast system to predict extreme
1213 weather events at high spatial and temporal resolution. Regarding the cyclone's trajectory, the
1214 EnKF provides a more realistic representation of the Qendresa's observed path.

1215
1216 Although the EnKF technique has shown in general better performance against the 3DVar for
1217 the two extreme weather events analyzed in this study, it is also important to account for the
1218 computational resources required by each method. The EnKF requires approximately, 36 times
1219 more model integrations per cycle than 3DVar's single forecast, in addition to the overhead of
1220 computing ensemble updates. This makes the 3DVar appealing because it is much faster and
1221 cheaper than the EnKF, and it makes this technique particularly suitable for operational
1222 purposes at the small weather forecast centers.

1223
1224
1225 An interesting result of this study is that, for highly non-Gaussian extreme events the
1226 deterministic 3DVar forecast can occasionally outperform the EnKF ensemble mean in terms
1227 of point forecasts (e.g., minimum central pressure), because averaging across ensemble
1228 members tends to smooth out the tails of a skewed probability distribution. In contrast,

Eliminado: 3DVar

Eliminado: much less

Eliminado: making 3DVar less expensive computationally.

Eliminado: computational resources than the EnKF because it does not need to build an ensemble of considerable size, and it does not need either to simulate model trajectories between the assimilation of a set of observations at time t

Eliminado: 1

Eliminado: and the subsequent set of observations valid at t_2 .

Eliminado: Another interesting result that we have shown in this study is that depending on the level of predictability of the weather event and its sensitivity to numerical physical parameterizations used to build the ensemble, the 3DVar performs better than the EnKF ensemble mean. We speculated that this is linked to the way the background error covariances from these two methods are built. Based on this, we suppose that a better approach could be to use Hybrid error covariance models, where the forecast error covariance matrix is obtained linearly combining the ensemble-based error covariance from the EnKF and the static climatological error covariance matrix from the 3DVar.

probabilistic metrics like ROC/AUC consistently favor the EnKF, reflecting its superior ability to capture forecast uncertainty. We attribute these contrasting behaviors to the different approaches to background error covariances: 3DVar employs a static covariance, while EnKF uses a flow-dependent covariance estimated from a finite ensemble. To combine the strengths of both methods, a hybrid error covariance approach—where the forecast error covariance matrix is formed by linearly blending the EnKF’s ensemble-derived covariances with the 3DVar’s static climatological covariances—may offer improved forecast skill for convective-scale extreme events.

Further work will investigate the impact of using hybrid DA schemes in comparison to standard 3DVar or EnKF. In this scenario, it is expected that the hybrid error covariance matrix will be more precise than the one derived from the ensemble members or from climatology, which on their own are not able to reproduce key aspects of challenging extreme weather events. High temporal and spatial observations from Doppler Weather radars, such as reflectivity and radial wind velocities, will be assimilated for this case to obtain accurate analysis and thus, improve the short-range forecast of this catastrophic flash-flood event. In addition, it is important to highlight that satellite-based data assimilation provides a significant opportunity for enhancing convective-scale forecasting, particularly in data-sparse maritime regions such as the Mediterranean, where the formation of extreme weather events like tropical-like cyclones is increasingly impacting densely populated areas. Future studies integrating high-resolution satellite observations, such as cloud top heights, thermodynamic profiles or cloud properties, could further enhance the accuracy of convective-scale predictions, improving early warning capabilities and disaster preparedness.

Acknowledgements:

The first author acknowledges the European Union’s Horizon 2020 research and innovation programme under the *Marie Skłodowska-Curie* grant agreement 101106403 [SENTINEL]. This research is also sponsored by the Ministerio de Ciencia e Innovación-Agencia Estatal de Investigación TRAMPAS (PID2020-113036RB-I00/AEI/10.13039/501100011033). The authors thankfully acknowledge Météo-France for supplying the data and HyMeX database teams (ESPRI/IPSL and SEDOO/OMP) for their help in accessing the data. The author also acknowledges the computer resources at MareNostrum IV and CRAY supercomputers, as well as the technical support provided by the Barcelona Supercomputer Center (RES-AECT-2017-1-0014, RES-AECT-2017-2-0014) and ECMWF data center, required to perform the high-resolution simulations presented in this study.

References

- Albergel, C., Zheng, Y., Bonan, B., Dutra, E., Rodríguez-Fernández, N., Munier, S., ... & Calvet, J. C. (2020). Data assimilation for continuous global assessment of severe conditions over terrestrial surfaces. *Hydrology and Earth System Sciences*, 24(9), 4291-4316.
- Amengual, A., Carrió, D. S., Ravazzani, G., & Homar, V. (2017). A comparison of ensemble strategies for flash flood forecasting: The 12 october 2007 case study in Valencia, Spain. *Journal of Hydrometeorology*, 18(4), 1143-1166.
- Amengual, A., Hermoso, A., Carrió, D. S., & Homar, V. (2021). The Sequence of Heavy Precipitation and Flash Flooding of 12 and 13 September 2019 in Eastern Spain. Part II: A Hydrometeorological Predictability Analysis Based on Convection-Permitting Ensemble Strategies. *Journal of Hydrometeorology*, 22(8), 2153-2177.
- Anderson, J. L., & Anderson, S. L. (1999). A Monte Carlo implementation of the nonlinear filtering problem to produce ensemble assimilations and forecasts. *Monthly weather review*, 127(12), 2741-2758.
- Anderson, J. L. (2001). An ensemble adjustment Kalman filter for data assimilation. *Monthly weather review*, 129(12), 2884-2903.
- Anderson, J. L., & Collins, N. (2007). Scalable implementations of ensemble filter algorithms for data assimilation. *Journal of Atmospheric and Oceanic Technology*, 24(8), 1452-1463.
- Anderson, J., Hoar, T., Raeder, K., Liu, H., Collins, N., Torn, R., & Avellano, A. (2009). The data assimilation research testbed: A community facility. *Bulletin of the American Meteorological Society*, 90(9), 1283-1296.
- Ballard, Susan P., et al. "Performance of 4D-Var NWP-based nowcasting of precipitation at the Met Office for summer 2012." *Quarterly Journal of the Royal Meteorological Society* 142.694 (2016): 472-487.
- Barker DM, Huang W, Guo Y-R, Bourgeois A, Xiao XN (2004) A three-dimensional variational data assimilation system for MM5: implementation and initial results. *Mon Wea Rev* 132:897–914
- Bowman, A. W., & Azzalini, A. (1997). *Applied smoothing techniques for data analysis: the kernel approach with S-Plus illustrations* (Vol. 18). OUP Oxford.
- Bryan, G. H., & Rotunno, R. (2005, October). Statistical convergence in simulated moist absolutely unstable layers. In *Preprints, 11th Conf. on Mesoscale Processes*, Albuquerque, NM, Amer. Meteor. Soc. M (Vol. 1).

1340
1341 Capecchi V, Antonini A, Benedetti R, Fibbi L, Melani S, Rovai L, Ricchi A, Cerrai D.
1342 Assimilating X- and S-Band Radar Data for a Heavy Precipitation Event in Italy. *Water*. 2021;
1343 13(13):1727. <https://doi.org/10.3390/w13131727>.
1344
1345 Carrassi, A., Bocquet, M., Bertino, L., & Evensen, G. (2018). Data assimilation in the
1346 geosciences: An overview of methods, issues, and perspectives. *Wiley Interdisciplinary*
1347 *Reviews: Climate Change*, 9(5), e535.
1348
1349 Carrió, D. S., & Homar, V. (2016). Potential of sequential EnKF for the short-range prediction
1350 of a maritime severe weather event. *Atmospheric Research*, 178, 426-444.
1351
1352 Carrió, D. S., Homar, V., Jansa, A., Romero, R., & Picornell, M. A. (2017). Tropicalization
1353 process of the 7 November 2014 Mediterranean cyclone: Numerical sensitivity study.
1354 *Atmospheric Research*, 197, 300-312.
1355
1356 Carrió, D. S., Homar, V., & Wheatley, D. M. (2019). Potential of an EnKF storm-scale data
1357 assimilation system over sparse observation regions with complex orography. *Atmospheric*
1358 *Research*, 216, 186-206.
1359
1360 Carrió, D. S., Bishop, C. H., & Kotsuki, S. (2021). Empirical determination of the covariance
1361 of forecast errors: An empirical justification and reformulation of hybrid covariance models.
1362 *Quarterly Journal of the Royal Meteorological Society*, 147(736), 2033-2052.
1363
1364 Carrió, D. S., Jansà, A., Homar, V., Romero, R., Rigo, T., Ramis, C., ... & Maimó, A. (2022).
1365 Exploring the benefits of a Hi-EnKF system to forecast an extreme weather event. The 9th
1366 October 2018 catastrophic flash flood in Mallorca. *Atmospheric Research*, 265, 105917.
1367
1368 Carrió, D. S. (2023): Improving the predictability of the Qendresa Mediane by the assimilation
1369 of conventional and atmospheric motion vector observations. Storm-scale analysis and short-
1370 range forecast, *Nat. Hazards Earth Syst. Sci. Discuss.* <https://doi.org/10.5194/nhess-2022-58>,
1371
1372 Cioni, G, Cerrai, D, Klocke, D. (2018). Investigating the predictability of a Mediterranean
1373 tropical-like cyclone using a storm-resolving model. *Q J R Meteorol Soc.*; 144: 1598– 1610.
1374 <https://doi.org/10.1002/qj.3322>
1375
1376 Clayton, A. M., Lorenc, A. C., & Barker, D. M. (2013). Operational implementation of a hybrid
1377 ensemble/4D-Var global data assimilation system at the Met Office. *Quarterly Journal of the*
1378 *Royal Meteorological Society*, 139(675), 1445-1461.
1379
1380 Corrales, P. B., Galligani, V., Ruiz, J., Sapucci, L., Dillon, M. E., Skabar, Y. G., ... & Nesbitt,
1381 S. W. (2023). Hourly assimilation of different sources of observations including satellite
1382 radiances in a mesoscale convective system case during RELAMPAGO campaign.
1383 *Atmospheric Research*, 281, 106456.
1384

1385 Courtier, P. H. I. L. I. P. P. E., Thépaut, J. N., & Hollingsworth, A. (1994). A strategy for
 1386 operational implementation of 4D-Var, using an incremental approach. *Quarterly Journal of*
 1387 *the Royal Meteorological Society*, 120(519), 1367-1387.

1388

1389 Di Muzio, E, Riemer, M, Fink, AH, Maier-Gerber, M. Assessing the predictability of
 1390 Medicanes in ECMWF ensemble forecasts using an object-based approach. *Q J R Meteorol*
 1391 *Soc.* 2019; 145: 1202– 1217. <https://doi.org/10.1002/qj.3489>

1392

1393 Dowell, D. C., Wicker, L. J., & Snyder, C. (2011). Ensemble Kalman filter assimilation of
 1394 radar observations of the 8 May 2003 Oklahoma City supercell: Influences of reflectivity
 1395 observations on storm-scale analyses. *Monthly Weather Review*, 139(1), 272-294.

1396

1397 Drobinski, P., Ducrocq, V., Alpert, P., Anagnostou, E., Béranger, K., Borga, M., ... & Wernli,
 1398 H. (2014). HyMeX: A 10-year multidisciplinary program on the Mediterranean water cycle.
 1399 *Bulletin of the American Meteorological Society*, 95(7), 1063-1082.

1400

1401 Dudhia, J. (1989). Numerical study of convection observed during the winter monsoon
 1402 experiment using a mesoscale two-dimensional model. *Journal of Atmospheric Sciences*,
 1403 46(20), 3077-3107.

1404

1405 Eliassen, A. (1954). Provisional report on calculation of spatial covariance and autocorrelation
 1406 of the pressure field. Peport no 5, Videnskaps-Akademiets Institutt for Vaer-Og
 1407 Klimaforskning, Oslo, Norway, 12.

1408

1409 Emanuel, K. (2005). Genesis and maintenance of" Mediterranean hurricanes". *Advances in*
 1410 *Geosciences*, 2, 217-220.

1411

1412 Evensen, G. (1994). Sequential data assimilation with a nonlinear quasi-geostrophic model
 1413 using Monte Carlo methods to forecast error statistics. *Journal of Geophysical Research:*
 1414 *Oceans*, 99(C5), 10143-10162.

1415

1416 Federico, S., Torcasio, R. C., Puca, S., Vulpiani, G., Comellas Prat, A., Dietrich, S., & Avolio,
 1417 E. (2021). Impact of radar reflectivity and lightning data assimilation on the rainfall forecast
 1418 and predictability of a summer convective thunderstorm in Southern Italy. *Atmosphere*, 12(8),
 1419 958.

1420

1421 Ferrer Hernández, A. L., González Jardines, P. M., Sierra Lorenzo, M., & de la Caridad Aguiar
 1422 Figueroa, D. (2022). Impact of the Assimilation of Non-Precipitating Echoes Reflectivity Data
 1423 on the Short-Term Numerical Forecast of SisPI. *Environmental Sciences Proceedings*, 19(1),
 1424 13.

1425

1426 Ferretti, R., Pichelli, E., Gentile, S., Maiello, I., Cimini, D., Davolio, S., ... & Rotunno, R.
 1427 (2014). Overview of the first HyMeX Special Observation Period over Italy: observations and
 1428 model results. *Hydrology and Earth System Sciences*, 18(5), 1953-1977.

1429

1430 Fitzpatrick, P. J., Li, Y., Hill, C., Karan, H., Lim, E., & Xiao, Q. (2007, June). The impact of
1431 radar data assimilation on a squall line in Mississippi. In 22nd Conference on Weather Analysis
1432 and Forecasting/18th Conference on Numerical Weather Prediction.

1433

1434 Flaounas, E., Lagouvardos, K., Kotroni, V., Claud, C., Delanoë, J., Flamant, C., ... & Wernli,
1435 H. (2016). Processes leading to heavy precipitation associated with two Mediterranean
1436 cyclones observed during the HyMeX SOP1. *Quarterly Journal of the Royal Meteorological
1437 Society*, 142, 275-286.

1438

1439 Fujita, T., Stensrud, D. J., & Dowell, D. C. (2007). Surface data assimilation using an ensemble
1440 Kalman filter approach with initial condition and model physics uncertainties. *Monthly
1441 weather review*, 135(5), 1846-1868.

1442

1443 Gao, J., Fu, C., Stensrud, D. J., & Kain, J. S. (2016). OSSEs for an ensemble 3DVAR data
1444 assimilation system with radar observations of convective storms. *Journal of the Atmospheric
1445 Sciences*, 73(6), 2403-2426.

1446

1447 Garcies, L., & Homar, V. (2009). Ensemble sensitivities of the real atmosphere: application to
1448 Mediterranean intense cyclones. *Tellus A: Dynamic Meteorology and Oceanography*, 61(3),
1449 394-406.

1450

1451 Gaspari, G., & Cohn, S. E. (1999). Construction of correlation functions in two and three
1452 dimensions. *Quarterly Journal of the Royal Meteorological Society*, 125(554), 723-757.

1453

1454 Grell, G. A., & Freitas, S. R. (2014). A scale and aerosol aware stochastic convective
1455 parameterization for weather and air quality modeling. *Atmospheric Chemistry and Physics*,
1456 14(10), 5233-5250.

1457

1458 Gustafsson, N., Janjić, T., Schraff, C., Leuenberger, D., Weissmann, M., Reich, H., ... & Fujita,
1459 T. (2018). Survey of data assimilation methods for convective-scale numerical weather
1460 prediction at operational centres. *Quarterly Journal of the Royal Meteorological Society*,
1461 144(713), 1218-1256.

1462

1463 Hacker, J. P., Anderson, J. L., & Pagowski, M. (2007). Improved vertical covariance estimates
1464 for ensemble-filter assimilation of near-surface observations. *Monthly Weather Review*,
1465 135(3), 1021-1036.

1466

1467 Hamill, T. M., & Snyder, C. (2000). A hybrid ensemble Kalman filter–3D variational analysis
1468 scheme. *Monthly Weather Review*, 128(8), 2905-2919.

1469

1470 Honda, T., Miyoshi, T., Lien, G. Y., Nishizawa, S., Yoshida, R., Adachi, S. A., ... & Bessho,
1471 K. (2018). Assimilating all-sky Himawari-8 satellite infrared radiances: A case of Typhoon
1472 Soudelor (2015). *Monthly Weather Review*, 146(1), 213-229.

1473

1474 Hong, S. Y., Noh, Y., & Dudhia, J. (2006). A new vertical diffusion package with an explicit
 1475 treatment of entrainment processes. *Monthly weather review*, 134(9), 2318-2341.
 1476
 1477 Houtekamer, P. L., & Mitchell, H. L. (1998). Data assimilation using an ensemble Kalman
 1478 filter technique. *Monthly Weather Review*, 126(3), 796-811.
 1479
 1480 Hu, Junjun, et al. "Assessment of Storm-Scale Real Time Assimilation of GOES-16 GLM
 1481 Lightning-Derived Water Vapor Mass on Short Term Precipitation Forecasts During the 2020
 1482 Spring Forecast Experiment." *Journal of Geophysical Research: Atmospheres* 126.21 (2021):
 1483 e2021JD034603.
 1484
 1485 Huang, X. Y., Xiao, Q., Barker, D. M., Zhang, X., Michalakes, J., Huang, W., ... & Kuo, Y. H.
 1486 (2009). Four-dimensional variational data assimilation for WRF: Formulation and preliminary
 1487 results. *Monthly Weather Review*, 137(1), 299-314.
 1488
 1489 Hung MK, Tien DD, Quan DD, Duc TA, Dung PTP, Hole LR, Nam HG. Assessments of Use
 1490 of Blended Radar–Numerical Weather Prediction Product in Short-Range Warning of Intense
 1491 Rainstorms in Localized Systems (SWIRLS) for Quantitative Precipitation Forecast of
 1492 Tropical Cyclone Landfall on Vietnam’s Coast. *Atmosphere*. 2023; 14(8):1201.
 1493 <https://doi.org/10.3390/atmos14081201>
 1494
 1495 Iacono, M. J., Delamere, J. S., Mlawer, E. J., Shephard, M. W., Clough, S. A., & Collins, W.
 1496 D. (2008). Radiative forcing by long-lived greenhouse gases: Calculations with the AER
 1497 radiative transfer models. *Journal of Geophysical Research: Atmospheres*, 113(D13).
 1498
 1499 Janjić, Z. I. (1990). The step-mountain coordinate: Physical package. *Monthly weather review*,
 1500 118(7), 1429-1443.
 1501
 1502 Janić, Z. I. (2001). Nonsingular implementation of the Mellor-Yamada level 2.5 scheme in the
 1503 NCEP Meso model.
 1504
 1505 Janjić, Tijana, Yuefei Zeng, and Yvonne Ruckstuhl. "Weakly Constrained LETKF for
 1506 Convective-Scale Data Assimilation." (2022).
 1507
 1508 Jansa, A., Alpert, P., Arbogast, P., Buzzi, A., Ivancan-Picek, B., Kotroni, V., ... & Speranza,
 1509 A. (2014). MEDEX: a general overview. *Natural Hazards and Earth System Sciences*, 14(8),
 1510 1965-1984.
 1511
 1512 Jones, T. A., Otkin, J. A., Stensrud, D. J., & Knopfmeier, K. (2013). Assimilation of satellite
 1513 infrared radiances and Doppler radar observations during a cool season observing system
 1514 simulation experiment. *Monthly weather review*, 141(10), 3273-3299.
 1515
 1516 Kain, J. S., & Fritsch, J. M. (1990). A one-dimensional entraining/detraining plume model and
 1517 its application in convective parameterization. *Journal of Atmospheric Sciences*, 47(23), 2784-
 1518 2802.

1519
1520 Kain, J. S. (2004). The Kain–Fritsch convective parameterization: an update. *Journal of applied*
1521 *meteorology*, 43(1), 170-181.
1522
1523 Kalnay, E. (2003). *Atmospheric modeling, data assimilation and predictability*. Cambridge
1524 university press.
1525
1526 Lagasio, M., Silvestro, F., Campo, L., & Parodi, A. (2019). Predictive Capability of a High-
1527 Resolution Hydrometeorological Forecasting Framework Coupling WRF Cycling 3DVAR and
1528 Continuum. *Journal of Hydrometeorology*, 20(7), 1307-1337. [https://doi.org/10.1175/JHM-D-](https://doi.org/10.1175/JHM-D-18-0219.1)
1529 18-0219.1
1530
1531 Le Dimet, F. X., & Talagrand, O. (1986). Variational algorithms for analysis and assimilation
1532 of meteorological observations: theoretical aspects. *Tellus A: Dynamic Meteorology and*
1533 *Oceanography*, 38(2), 97-110.
1534
1535 Lee, J. H., Lee, H. H., Choi, Y., Kim, H. W., & Lee, D. K. (2010). Radar data assimilation for
1536 the simulation of mesoscale convective systems. *Advances in Atmospheric Sciences*, 27, 1025-
1537 1042.
1538
1539 Li, X., J. Ming, M. Xue, Y. Wang, and K. Zhao, 2015: Implementation of a dynamic equation
1540 constraint based on the steady state momentum equations within the WRF hybrid ensemble-
1541 3DVar data assimilation system and test with radar T-TREC wind assimilation for tropical
1542 Cyclone Chanthu (2010). *J. Geophys. Res. Atmos.*, 120, 4017–4039, doi:
1543 10.1002/2014JD022706.
1544
1545 Li, X., Zeng, M., Wang, Y., Wang, W., Wu, H., & Mei, H. (2016). Evaluation of two
1546 momentum control variable schemes and their impact on the variational assimilation of
1547 radarwind data: Case study of a squall line. *Advances in Atmospheric Sciences*, 33, 1143-1157.
1548
1549 Lorenc, A. C. (1981). A global three-dimensional multivariate statistical interpolation scheme.
1550 *Monthly Weather Review*, 109(4), 701-721.
1551
1552 Lorenc, A. C. (1986). Analysis methods for numerical weather prediction. *Quarterly Journal*
1553 *of the Royal Meteorological Society*, 112(474), 1177-1194.
1554
1555 Lorenc, A. C. (2003). The potential of the ensemble Kalman filter for NWP—A comparison
1556 with 4D-Var. *Quarterly Journal of the Royal Meteorological Society: A journal of the*
1557 *atmospheric sciences, applied meteorology and physical oceanography*, 129(595), 3183-3203.
1558
1559 Llasat, M., & Sempere-Torres, D. (2001). Heavy rains and floods in west mediterranean areas:
1560 a climatic feature. *Geophysical Research Abstr acts*, 3.
1561

1562 Llasat, M. C., Llasat-Botija, M., Prat, M. A., Porcu, F., Price, C., Mugnai, A., ... & Nicolaides,
 1563 K. (2010). High-impact floods and flash floods in Mediterranean countries: the FLASH
 1564 preliminary database. *Advances in Geosciences*, 23, 47-55.
 1565
 1566 Mason, I., 1982: A model for assessment of weather forecasts. *Aust. Met. Mag.*, 30, 291-303.
 1567
 1568 Mass, C. F., Ovens, D., Westrick, K., & Colle, B. A. (2002). Does increasing horizontal
 1569 resolution produce more skillful forecasts?: The Results of Two Years of real-Time Numerical
 1570 Weather Prediction over the Pacific Northwest. *Bulletin of the American Meteorological*
 1571 *Society*, 83(3), 407-430.
 1572
 1573 Mazzarella, V.; Maiello, I.; Ferretti, R.; Capozzi, V.; Picciotti, E.; Alberoni, P.; Marzano, F.;
 1574 Budillon, G. Reflectivity and velocity radar data assimilation for two flash flood events in
 1575 central Italy: A comparison between 3D and 4D variational methods. *Q. J. R. Meteorol. Soc.*
 1576 2020, 146, 348–366.
 1577
 1578 Mazzarella, V., Ferretti, R., Picciotti, E., & Marzano, F. S. (2021). Investigating 3D and 4D
 1579 variational rapid-update-cycling assimilation of weather radar reflectivity for a heavy rain
 1580 event in central Italy. *Natural Hazards and Earth System Sciences*, 21(9), 2849-2865.
 1581
 1582 Mittermaier, M., & Roberts, N. (2010). Intercomparison of spatial forecast verification
 1583 methods: Identifying skillful spatial scales using the fractions skill score. *Weather and*
 1584 *Forecasting*, 25(1), 343-354.
 1585
 1586 Nakanishi, M., & Niino, H. (2006). An improved Mellor–Yamada level-3 model: Its numerical
 1587 stability and application to a regional prediction of advection fog. *Boundary-Layer*
 1588 *Meteorology*, 119, 397-407.
 1589
 1590 Nakanishi, M., & Niino, H. (2009). Development of an improved turbulence closure model for
 1591 the atmospheric boundary layer. *Journal of the Meteorological Society of Japan. Ser. II*, 87(5),
 1592 895-912.
 1593
 1594 Pakalidou, N., & Karacosta, P. (2018). Study of very long-period extreme precipitation records
 1595 in Thessaloniki, Greece. *Atmospheric Research*, 208, 106-115.
 1596
 1597 Park, S. K., & Županski, D. (2003). Four-dimensional variational data assimilation for
 1598 mesoscale and storm-scale applications. *Meteorology and Atmospheric Physics*, 82(1), 173-
 1599 208.
 1600
 1601 Parrish, D., and J. Derber, 1992: The National Meteorological Center's spectral statistical-
 1602 interpolation analysis system. *Mon. Wea. Rev.*, 120, 1747–1763, doi:10.1175/1520-
 1603 0493(1992)120<1747:TNMCSS>2.0.CO;2.
 1604

1605 Petterssen, S. (1956). Weather analysis and forecasting: motion and motion systems. McGraw-
 1606 Hill.
 1607
 1608 Pichelli, E., Rotunno, R. and Ferretti, R. (2017), Effects of the Alps and Apennines on forecasts
 1609 for Po Valley convection in two HyMeX cases. Q.J.R. Meteorol. Soc., 143: 2420-2435.
 1610 <https://doi.org/10.1002/qj.3096>
 1611
 1612 Poterjoy, J. (2016). A localized particle filter for high-dimensional nonlinear systems. Monthly
 1613 Weather Review, 144(1), 59-76.
 1614
 1615 Pu, Z., Li, X., Velden, C. S., Aberson, S. D., & Liu, W. T. (2008). The impact of aircraft
 1616 dropsonde and satellite wind data on numerical simulations of two landfalling tropical storms
 1617 during the tropical cloud systems and processes experiment. Weather and Forecasting, 23(1),
 1618 62-79.
 1619
 1620 Pytharoulis, I., Matsangouras, I. T., Tegoulis, I., Kotsopoulos, S., Karacostas, T. S., & Nastos,
 1621 P. T. (2017). Numerical study of the medicane of November 2014. In Perspectives on
 1622 Atmospheric Sciences (pp. 115-121). Springer International Publishing.
 1623
 1624 Pytharoulis, I. (2018). Analysis of a Mediterranean tropical-like cyclone and its sensitivity to
 1625 the sea surface temperatures. Atmospheric Research, 208, 167-179.
 1626
 1627 Rabier, F., Järvinen, H., Klinker, E., Mahfouf, J. F., & Simmons, A. (2000). The ECMWF
 1628 operational implementation of four-dimensional variational assimilation. I: Experimental
 1629 results with simplified physics. Quarterly Journal of the Royal Meteorological Society,
 1630 126(564), 1143-1170.
 1631
 1632 Rawlins, F., Ballard, S. P., Bovis, K. J., Clayton, A. M., Li, D., Inverarity, G. W., ... & Payne,
 1633 T. J. (2007). The Met Office global four-dimensional variational data assimilation scheme.
 1634 Quarterly Journal of the Royal Meteorological Society: A journal of the atmospheric sciences,
 1635 applied meteorology and physical oceanography, 133(623), 347-362.
 1636
 1637 Roberts, N.M. (2003) The impact of a change to the use of the convection scheme to high-
 1638 resolution simulations of convective events. Met Office Forecasting Research Technical Report
 1639 number: 407.
 1640
 1641 Roberts, N. M., & Lean, H. W. (2008). Scale-selective verification of rainfall accumulations
 1642 from high-resolution forecasts of convective events. Monthly Weather Review, 136(1), 78-97.
 1643
 1644 Romero, R., Guijarro, J. A., Ramis, C., & Alonso, S. (1998). A 30-year (1964–1993) daily
 1645 rainfall data base for the Spanish Mediterranean regions: First exploratory study. International
 1646 Journal of Climatology: A Journal of the Royal Meteorological Society, 18(5), 541-560.
 1647

Romine, G. S., Schwartz, C. S., Snyder, C., Anderson, J. L., & Weisman, M. L. (2013). Model bias in a continuously cycled assimilation system and its influence on convection-permitting forecasts. *Monthly weather review*, 141(4), 1263-1284.

Schwartz, C. S., Kain, J. S., Weiss, S. J., Xue, M., Bright, D. R., Kong, F., ... & Wandishin, M. S. (2010). Toward improved convection-allowing ensembles: Model physics sensitivities and optimizing probabilistic guidance with small ensemble membership. *Weather and Forecasting*, 25(1), 263-280.

Scott, D. W. (2015). *Multivariate density estimation: theory, practice, and visualization*. John Wiley & Sons.

Shen, F., Song, L., Li, H., He, Z., & Xu, D. (2022). Effects of different momentum control variables in radar data assimilation on the analysis and forecast of strong convective systems under the background of northeast cold vortex. *Atmospheric Research*, 280, 106415.

Silverman, B. W. (2018). *Density estimation for statistics and data analysis*. Routledge.

Skamarock, W. C., Klemp, J. B., Dudhia, J., Gill, D. O., Barker, D. M., Wang, W., & Powers, J. G. (2008). A description of the advanced research WRF version 3. National Center For Atmospheric Research Boulder Co Mesoscale and Microscale Meteorology Div.

Stanski, H.R., L.J. Wilson, and W.R. Burrows, 1989: Survey of common verification methods in meteorology. World Weather Watch Tech. Rept. No.8, WMO/TD No.358, WMO, Geneva, 114 pp.

Stensrud, D. J., Bao, J. W., & Warner, T. T. (2000). Using initial condition and model physics perturbations in short-range ensemble simulations of mesoscale convective systems. *Monthly Weather Review*, 128(7), 2077-2107.

Stensrud, D. J., Xue, M., Wicker, L. J., Kelleher, K. E., Foster, M. P., Schaefer, J. T., ... & Tuell, J. P. (2009). Convective-scale warn-on-forecast system: A vision for 2020. *Bulletin of the American Meteorological Society*, 90(10), 1487-1500.

Sun, J., & Crook, N. A. (1997). Dynamical and microphysical retrieval from Doppler radar observations using a cloud model and its adjoint. Part I: Model development and simulated data experiments. *Journal of the Atmospheric Sciences*, 54(12), 1642-1661.

Swets, J. A. (1973). The Relative Operating Characteristic in Psychology: A technique for isolating effects of response bias finds wide use in the study of perception and cognition. *Science*, 182(4116), 990-1000.

Tewari, M., Chen, M., Wang, F., Dudhia, W., LeMone, J., Mitchell, K., Ek, M., Gayno, G., Wegiel, J., and Cuenca, R. H. (2004, January). Implementation and verification of the unified

1692 NOAH land surface model in the WRF model (Formerly Paper Number 17.5). In Proceedings
1693 of the 20th conference on weather analysis and forecasting/16th conference on numerical
1694 weather prediction, Seattle, WA, USA (Vol. 14).
1695
1696 Taylor, K. E. (2001). Summarizing multiple aspects of model performance in a single diagram.
1697 Journal of geophysical research: atmospheres, 106(D7), 7183-7192.
1698
1699 Tiedtke, M. I. C. H. A. E. L. (1989). A comprehensive mass flux scheme for cumulus
1700 parameterization in large-scale models. Monthly weather review, 117(8), 1779-1800.
1701
1702 Thompson, G., Field, P. R., Rasmussen, R. M., & Hall, W. D. (2008). Explicit forecasts of
1703 winter precipitation using an improved bulk microphysics scheme. Part II: Implementation of
1704 a new snow parameterization. Monthly Weather Review, 136(12), 5095-5115.
1705
1706 Tong, M., & Xue, M. (2005). Ensemble Kalman filter assimilation of Doppler radar data with
1707 a compressible nonhydrostatic model: OSS experiments. Monthly Weather Review, 133(7),
1708 1789-1807.
1709
1710 Torcasio, R. C., Federico, S., Comellas Prat, A., Panegrossi, G., D'Adderio, L. P., & Dietrich,
1711 S. (2021). Impact of lightning data assimilation on the short-term precipitation forecast over
1712 the Central Mediterranean Sea. Remote Sensing, 13(4), 682.
1713
1714 Tukey, J. W. (1977). Exploratory data analysis (Vol. 2, pp. 131-160).
1715
1716 Van Leeuwen, P. J. (2009). Particle filtering in geophysical systems. Monthly Weather Review,
1717 137(12), 4089-4114.
1718
1719 Velden, C., Lewis, W. E., Bresky, W., Stettner, D., Daniels, J., & Wanzong, S. (2017).
1720 Assimilation of high-resolution satellite-derived atmospheric motion vectors: Impact on
1721 HWRF forecasts of tropical cyclone track and intensity. Monthly Weather Review, 145(3),
1722 1107-1125.
1723
1724 Wang, H., Huang, X. Y., Sun, J., Xu, D., Fan, S., Zhong, J., & Zhang, M. (2013, September).
1725 A comparison between the 3/4DVAR and hybrid ensemble-VAR techniques for radar data
1726 assimilation. In 35th Conference on Radar Meteorology, Breckenridge.
1727
1728 Wang, Y., Yussouf, N., Kerr, C. A., Stratman, D. R., & Matilla, B. C. (2022). An experimental
1729 1-km Warn-on-Forecast System for hazardous weather events. Monthly Weather Review,
1730 150(11), 3081-3102.
1731
1732 Wheatley, D. M., Stensrud, D. J., Dowell, D. C., & Yussouf, N. (2012). Application of a WRF
1733 mesoscale data assimilation system to springtime severe weather events 2007–09. Monthly
1734 weather review, 140(5), 1539-1557.
1735

1736 Whitaker, J. S., Hamill, T. M., Wei, X., Song, Y., & Toth, Z. (2008). Ensemble data
1737 assimilation with the NCEP global forecast system. *Monthly Weather Review*, 136(2), 463-
1738 482.
1739
1740 Wu, X., Zhang, S., Liu, Z., Rosati, A., & Delworth, T. L. (2013). A study of impact of the
1741 geographic dependence of observing system on parameter estimation with an intermediate
1742 coupled model. *Climate Dynamics*, 40, 1789-1798.
1743
1744 Xiao, Q., & Sun, J. (2007). Multiple-radar data assimilation and short-range quantitative
1745 precipitation forecasting of a squall line observed during IHOP_2002. *Monthly Weather*
1746 *Review*, 135(10), 3381-3404.
1747
1748 Yano, J. I., Ziemiański, M. Z., Cullen, M., Termonia, P., Onvlee, J., Bengtsson, L., ... &
1749 Wyszogrodzki, A. A. (2018). Scientific challenges of convective-scale numerical weather
1750 prediction. *Bulletin of the American Meteorological Society*, 99(4), 699-710.
1751
1752 Yussouf, N., Dowell, D. C., Wicker, L. J., Knopfmeier, K. H., & Wheatley, D. M. (2015).
1753 Storm-scale data assimilation and ensemble forecasts for the 27 April 2011 severe weather
1754 outbreak in Alabama. *Monthly Weather Review*, 143(8), 3044-3066.
1755
1756
1757
1758
1759
1760
1761
1762
1763
1764
1765
1766
1767
1768
1769
1770
1771
1772
1773
1774
1775
1776
1777
1778
1779
1780
1781

Appendix

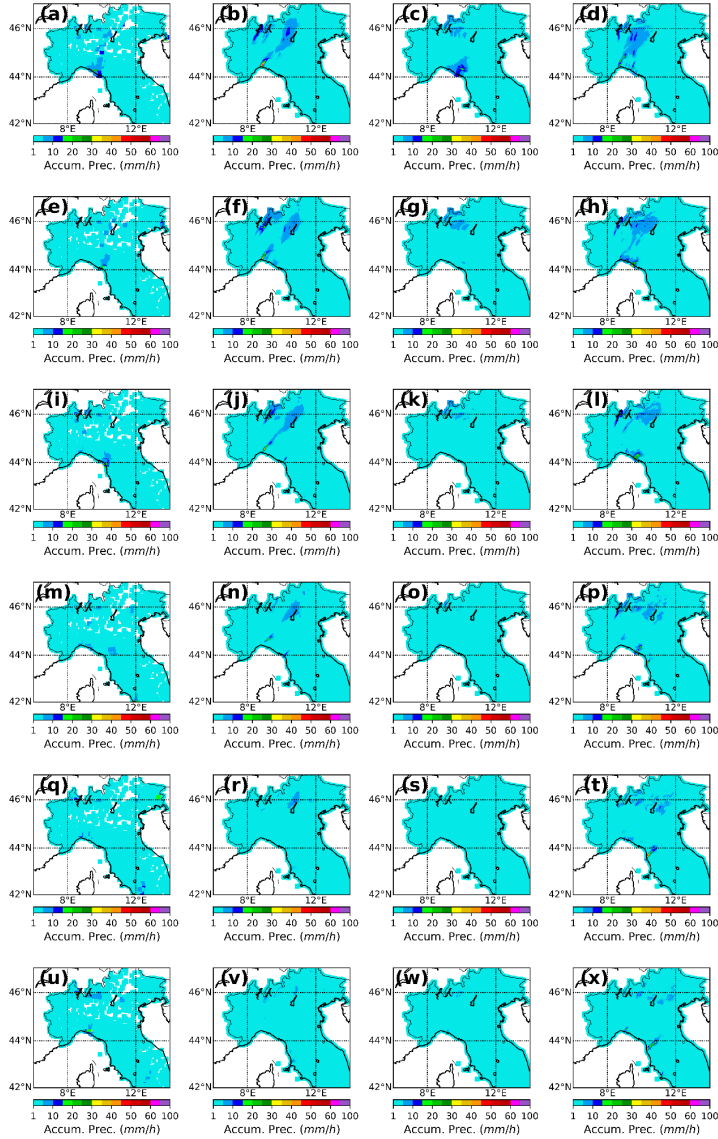


Fig. A1. 1-h accumulated precipitation computed from 00-06 UTC 15 October 2012 associated with Observations (first column), NODA (second column), EnKF (CNTRL) (third column) and 3DVar (CNTRL) (fourth column).

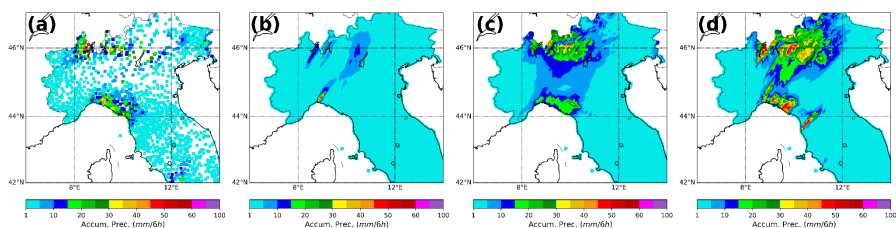


Fig. A2. 6-h accumulated precipitation computed from 00-06 UTC 15 October 2012 associated with (a) Observations, (b) NODA, (c) EnKF (CNTRL), (d) 3DVar (CNTRL).

Author Contribution

D. S. Carrió: Conceptualization, Methodology, Software, Validation, Formal analysis, investigation, writing-original draft, writing-review & editing, visualization, supervision; **V. Mazarella:** formal analysis, writing-review; **R. Ferretti:** formal analysis, writing-review, supervision.

Competing Interests

The authors declare that they have no conflict of interest.